Cálculo III - 2014

Exercício extra de Páscoa

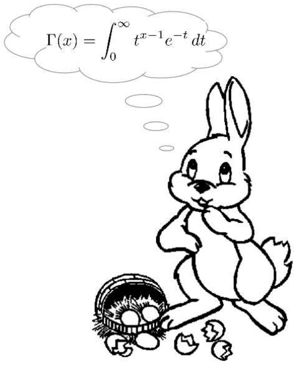

A função $\Gamma(x)$ e as bacias de atração de pontos fixos

Resumo

O título sugere uma relação que não existe... São dois problemas diferentes: a função $\Gamma(x)$ e as bacias de atração de pontos fixos de EDO...

1 A função $\Gamma(x)$

Como conversamos em aula, a função $\Gamma(x)$ é definida como

$$\Gamma(x) = \int_0^\infty t^{x-1} e^{-t}\, dx. \tag{1}$$

No contexto das transformadas de Laplace, a função $\Gamma(x)$ é util porque nos permite estender o resultado

$$\mathcal{L}[t^n] = \frac{n!}{s^{n+1}} \tag{2}$$

para n não inteiro. Vejamos:

$$\mathcal{L}[t^\alpha] = \int_0^\infty t^\alpha e^{-st}\, dt, \tag{3}$$

para $\alpha \in \mathbb{R}$ pode ser escrita, mediante a troca de variáveis $st = \tau$ e supondo, como sempre, $s > 0$,

$$\mathcal{L}[t^\alpha] = \frac{1}{s^{\alpha+1}} \int_0^\infty \tau^\alpha e^{-\tau}\, d\tau = \frac{\Gamma(\alpha+1)}{s^{\alpha+1}}, \tag{4}$$

de onde se obtem, diretamente, que $\Gamma(n) = (n-1)!$ para n inteiro positivo. Note que esta definição é compatível com $0! = 1$.

A função $\Gamma(x)$ não pode ser expressa a partir de funções elementares. Porém, ela tem várias propriedades que permitem que inferamos seu comportamento para todo $x \in \mathbb{R}$. Esta primeira parte do Exercício de Páscoa é a demonstração de várias dessas propriedades com a finalidade de contruirmos a função $\Gamma(x)$ para todo $x \in \mathbb{R}$. São estas:

1. Mostre que $\Gamma(x)$ satisfaz a seguinte relação funcional $\Gamma(x+1) = x\Gamma(x)$, para $x > 0$. Use esta propriedade para estender $\Gamma(x)$ para todo x real positivo a partir, por exemplo, dos valores de $\Gamma(x)$ no intervalo $(0, 1]$.

2. Mostre que $\lim_{x\to 0^+} \Gamma(x) \to \infty$.

3. Mostre que $\Gamma\left(\frac{1}{2}\right) = \sqrt{\pi}$. (Dica: reduza o problema ao cálculo da integral gaussiana).

4. Mostre que $\Gamma''(x) > 0$ para $x > 0$ e esboce o gráfico de $\Gamma(x)$ para $x > 0$.

5. Estime a localização do ponto de mínimo de $\Gamma(x)$ para $x > 0$.

6. Mostre que a definição original da função $\Gamma(x)$ (1) não converge para nenhum $x \leq 0$ (mostre que a correspondente integral imprópria não existe).

7. Apesar do resultado do item anterior, mostre que a relação funcional $\Gamma(x+1) = x\Gamma(x)$ pode ser usada para se definir $\Gamma(x)$ para $x < 0$. Mostre, em particular, que $\Gamma\left(-\frac{1}{2}\right) = -2\sqrt{\pi}$. Esboce o gráfico de $\Gamma(x)$ para todo $x \in \mathbb{R}$.

8. Estime o máximo local de $\Gamma(x)$ para $-1 < x < 0$.

2 Um sistema dissipativo simples

Nesta segunda parte do Exercício de Páscoa, consideraremos o sistema mecânico unidimensional correspondente a um corpo puntiforme de massa m movendo-se sob ação de um potencial $V(x)$ e de uma força de atrito $F_{\text{atr}} = -b\dot{x}$. A segunda lei de Newton, neste caso, será dada por

$$m\ddot{x} + b\dot{x} + V'(x) = 0. \tag{5}$$

Na ausência de atrito ($b = 0$), sabe-se que a energia total

$$E(t) = m\frac{\dot{x}(t)^2}{2} + V(x(t)) \tag{6}$$

é uma constante do movimento. Devido ao atrito, porém, a energia E não se manterá constante e irá decrescer com o tempo. Suponha um potencial $V(x)$ como o da Fig. 1. Este potencial possui três pontos de equilíbrio ($V' = 0$): dois estáveis ($V'' > 0$): A e C; um instável ($V'' < 0$): B. Dadas certas condições iniciais $x(0)$ e $\dot{x}(0)$ e, conseqüentemente, uma certa energia inicial $E(0)$, o sistema evoluirá de acordo com (5), perdendo energia continuamente devido à força de atrito e terminará, inexoravelmente, em repouso em um dos três pontos de equilíbrio. Intuitivamente, sabemos que somente para condições iniciais cuidadosamente escolhidas o sistema terminará no ponto instável B. Já os pontos estáveis deverão ser atingidos para um conjunto muito maior e menos restrito de condições iniciais. Chamaremos de *Bacia de*

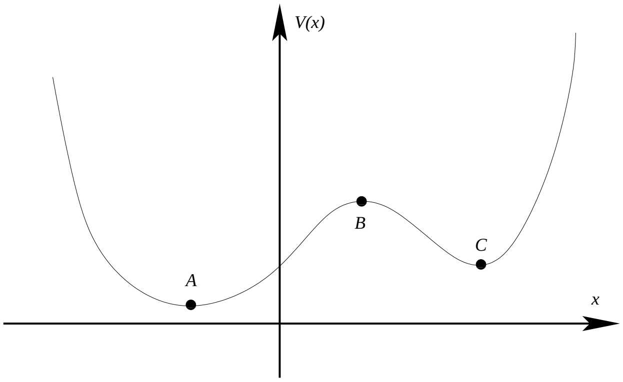

Figura 1: *Potencial* $V(x)$.

Atração de um certo ponto de equilíbrio $\bar{x}$ o conjunto de condições iniciais $(x_0, \dot{x}_0)$ no plano $(x, \dot{x})$ tal que as equações (5) quando resolvidas com as condições iniciais $x(0) = x_0$ e $\dot{x}(0) = \dot{x}_0$ levam a

$$\lim_{t\to\infty} x(t) = \bar{x}. \tag{7}$$

O objetivo deste exercício é identificar as bacias de atração no plano $(x, \dot{x})$ dos pontos de equilíbrio de um dado pontencial $V(x)$. As bacias deverão ser identificadas por cores diferentes de acordo com os pontos de equilíbrio correspondentes. Deve-se seguir o seguinte roteiro:

1. Encontre a expressão analítica de um potencial como o da Fig. 1.
2. Discretize o plano das condições iniciais $(x, \dot{x})$ em, por exemplo, 400×400 pontos.
3. Resolva *numericamente*[1] o problema de valor inicial da Eq. (5) para todos os pontos do plano das condições iniciais $(x, \dot{x})$ e gere as respectivas bacias de atração. Estabeleça um critério mais eficiente que (7) para decidir quando uma solução vai terminar num certo ponto de equilíbrio $\bar{x}$.

Há um artigo em anexo para os que queiram se aprofundar neste assunto. Obviamente, não faz parte do Exercício se aprofundar no artigo...

---

[1] A solução numérica de EDOs é um capítulo riquíssimo da Análise Numérica. Neste problema, porém, vocês devem usar algum pacote "profissional". Espero que este problema sirva de motivação para que vocês estudem MS211!

Physica 17D (1985) 125–153
North-Holland, Amsterdam

FRACTAL BASIN BOUNDARIES

Steven W. McDONALD,[a] Celso GREBOGI,[a] Edward OTT[a,b] and James A. YORKE[c]

Received 9 November 1984
Revised manuscript received 13 April 1985

Basin boundaries for dynamical systems can be either smooth or fractal. This paper investigates fractal basin boundaries. One practical consequence of such boundaries is that they can lead to great difficulty in predicting to which attractor a system eventually goes. The structure of fractal basin boundaries can be classified as being either locally connected or locally disconnected. Examples and discussion of both types of structures are given, and it appears that fractal basin boundaries should be common in typical dynamical systems. Lyapunov numbers and the dimension for the measure generated by inverse orbits are also discussed.

1. Introduction

Much of the interest in nonlinear dynamical systems has focused on the existence of periodic, quasiperiodic, and chaotic attractors, and the investigation of how these arise [1]. It is also important to recognize, however, that the analysis of a typical dissipative dynamical system may be complicated by the fact that initial conditions in different regions of phase space may generate orbits which exhibit different time-asymptotic behavior. That is, it is possible, and even common, that at fixed values of system parameters, more than one attractor may be present. The set of initial conditions (more precisely, the closure of this set) which eventually approach each particular attractor is called its basin of attraction. In this paper, we will be interested in the variety and structure of the boundaries which separate basins of attraction.

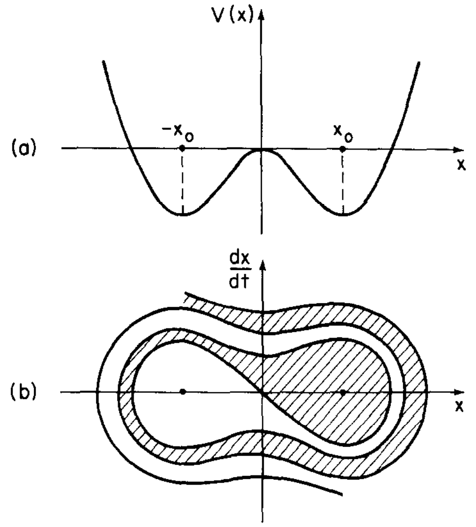

Fig. 1. (a) Potential $V(x)$ for a point particle moving in one dimension. With friction, almost every initial condition eventually comes to rest at one of the equilibrium points, x_0 or $-x_0$. (b) Phase (velocity-position) space for the system in (a). The basin of attraction for x_0 (crosshatched) is separated from the basin of attraction for $-x_0$ (blank) by a smooth basin boundary curve.

In order to illustrate the concepts of coexisting attractors, basins of attraction and basin boundaries, consider the simple case of a point particle moving under the influence of friction in a potential $V(x)$ as shown in fig. 1a. For almost any initial condition, the orbit will eventually come to rest at either of the two stable fixed points at $x = \pm x_0$. Fig. 1b schematically depicts the phase

---

[a] Laboratory for Plasma and Fusion Energy Studies, University of Maryland, College Park, MD 20742, USA.
[b] Department of Electrical Engineering and Department of Physics and Astronomy, University of Maryland, College Park, MD 20742, USA.
[c] Department of Mathematics and Institute for Physical Sciences and Technology, University of Maryland, College Park, MD 20742, USA.

0167-2789/85/$03.30 © Elsevier Science Publishers B.V.
(North-Holland Physics Publishing Division)

space of the system and the basins of attraction of these two fixed point attractors. An initial condition chosen in the crosshatched region eventually comes to rest at $x = x_0$, while any initial condition in the blank region tends to $x = -x_0$. The boundary separating these basins is the smooth curve passing through the origin. Points on the boundary do not tend to any attractor and so must be mapped to other boundary points: the basin boundary is an invariant set under the system action. In the example of fig. 1, initial conditions on the boundary approach the unstable fixed point at the origin (*not* an attractor); i.e., the boundary is the stable manifold of an unstable orbit (although this will not always be the case).

Another property of the boundary in fig. 1 is that it is a smooth curve. It is a main point of this paper that a basin boundary need not be a smooth curve or surface. Indeed, for a wide variety of systems it is common for boundaries to exhibit a fractal structure and to be characterized by a noninteger dimension.

The importance of studying the structure of basin boundaries is illustrated by the following example. Consider the simple two-dimensional phase space diagram schematically depicted in fig. 2. There are two possible final states, or attractors, denoted by A and B. The region to the left (right) of the basin boundary Σ is the basin of attraction for attractor A (or B, respectively). Let us consider an initial condition and measure its coordinates. Now suppose that this measurement has an uncertainty ε in the sense that the actual initial condition might be anywhere in a disc of radius ε centered at the measured value. In fig. 2, points 1 and 2 represent two such measured initial conditions. While the orbit generated by initial condition 1 is definitely attracted to B, initial condition 2 is uncertain in that it may be attracted to either A or B. Now assume that initial conditions are chosen randomly with uniform distribution in the rectangular region shown in fig. 2. We consider the fraction $f(\varepsilon)$ of initial conditions which are uncertain as to which attractor is approached when there is an initial error ε. For the simple case of fig. 2, initial conditions within a strip of width 2ε centered on the boundary are uncertain; thus, $f(\varepsilon)$ is proportional to ε. In section 2, however, we demonstrate that systems with fractal boundaries are more sensitive to initial uncertainty and can obey

$$f \sim \varepsilon^{\alpha}, \tag{1.1}$$

where α is *less than one*. We call α the *uncertainty exponent* and we say that these systems possess *final state sensitivity* [2]. We believe that many typical dynamical systems exhibit this behavior. In cases where the uncertainty exponent α is significantly less than unity, a substantial reduction in the error in the initial condition, ε, produces only a relatively small decrease in the uncertainty of the final state as measured by f. Furthermore, we show that the uncertainty exponent α is the difference between the dimension of the phase space and the "capacity dimension" of the basin boundary. This is explained in section 2 (cf. eq. (2.5) for a definition of capacity dimension). The increased sensitivity of final states to initial condition error when $\alpha < 1$ provides an important motivation for the study of fractal basin boundaries.

Another reason for interest in fractal basin boundaries is that as a system parameter is varied, a chaotic attractor can be suddenly destroyed in a collision with the basin boundary (we have called such events *crises* [3]); for values of the parameter beyond the crisis point, long chaotic transients occur [4]. Variation of the parameter in the opposite direction produces the creation of a chaotic attractor (a "route to chaos").

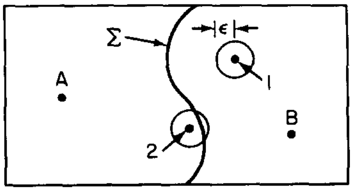

Fig. 2. A schematic region of phase space divided by the basin boundary Σ into basins of attraction for the two attractors A and B. Points 1 and 2 represent two initial conditions with uncertainty ε.

Several standard dissipative dynamical systems possess fractal basin boundaries. The work of Cartwright and Littlewood [5], Levinson [6], and Levi [7] can be shown to imply that the forced Van der Pol oscillator exhibits a fractal boundary due to the existence of a "horseshoe" in the dynamics. A similar analysis by Kaplan and Yorke [8] of the Lorenz system [9] of ordinary differential equations can also be shown (section 4.2) to imply the existence of a fractal basin boundary in a parameter regime below that at which the creation of the strange attractor occurs. Finally, we show that the simple one-dimensional logistic map possesses a fractal boundary in the period three regime [10] (or rather the third iterate of the map does). These examples are discussed in section 4, and it is shown that in these cases the basin boundary exhibits a fractal Cantor set structure. The basin structure of a simple two-dimensional mapping which models this behavior is shown in fig. 3a. Here there are two fixed point attractors ($A^{\pm}$); initial conditions in the dark region are attracted to A^{+}, while the blank region is the basin for A^{-}. The fine-scale complexity of this type of fractal boundary is further revealed under magnification in fig. 3b. (Note that the graininess in fig. 3 is due to finite resolution; i.e., fig. 3b should be regarded as consisting of an infinite number of dark and blank strips.)

The basin boundary in fig. 3 is not a continuous curve. In contrast, we observe in section 4 that fractal boundaries in two-dimensional maps can be continuous curves. This type of boundary is also "Cantor-like": a typical smooth curve crossing the boundary intersects it in an uncountable set that contains no segments. See section 3 for further discussion and classification of different types of fractal basin boundaries.

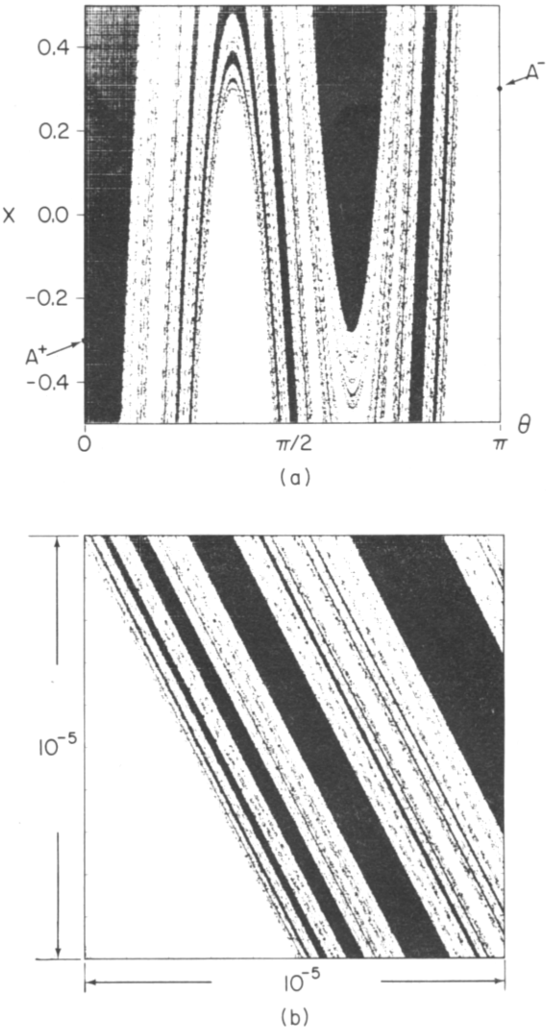

Fig. 3. (a) Basins of attraction for the two attractors A^+ (dark region) and A^- (blank region). This two-dimensional system is governed by the mapping in eqs. (4.1). (b) Magnification by a factor of 10^5 of the region in (a) given by $1.92200 \leq \theta \leq 1.92201$ and $-0.50000 \leq x \leq -0.49999$.

Perhaps the best-known examples [11] of boundaries which are fractal curves are found in two-dimensional dynamics of the form $z \to F(z)$, where F is an analytic function of the complex variable $z = x + iy$. Fig. 4a shows the complex plane divided into the two basins of the analytic map given by $F(z) = z^2 + 0.9z\exp(2\pi i\Omega)$, with $\Omega = (\sqrt{5}+1)/2$, the golden mean. Here, orbits originating in the interior blank region are attracted to the fixed point at the origin, whereas the dark region is the set of points which escape to infinity (the basin for the point at infinity). The boundary separating these regions is quite complicated and has "snowflake" structure on arbitrarily small scale, as suggested by the magnification in fig. 4b. Such boundaries can be classed as "quasi-circles" (see sections 3 and 5 for a defini-

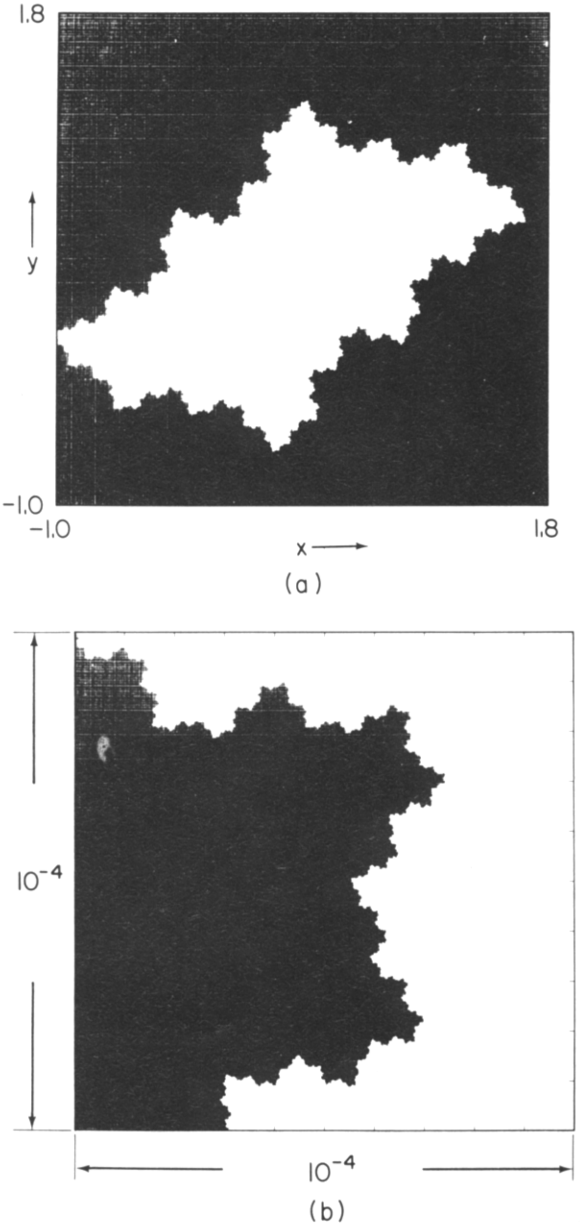

Fig. 4. (a) Basins of attraction for the fixed point at the origin (blank region) and the point at infinity (dark region). The mapping is given by the analytic function $z_{n+1} = z_n^2 + 0.9 z_n \exp(2\pi i \Omega)$, where $z \equiv x + iy$ and Ω is the golden mean. (b) Magnification by a factor of 10^4 of the region in (a) $0.72809 \leq x \leq 0.72819$, $0.02209 \leq y \leq 0.02219$.

tion and discussion of quasicircles), fractal curves that have a moderate degree of regularity.

Complex analytic maps are a very restricted class and possess special features not typical of two-dimensional maps in general. In particular, as a consequence of their Cauchy–Riemann structure they do not have chaotic attractors (the two Lyapunov numbers are equal). In section 5, therefore, we shall also study more general maps of the plane that provide more suitable models of typical nonlinear physical systems (possibly of higher dimension). These more general maps yield basin boundaries which are curves but lack the quasicircle property. An example of this more general set of maps is shown in fig. 5a. The blank region consists of initial conditions which are attracted to a chaotic attractor (which is also shown) and again, the dark region is the basin of attraction for the point at infinity. The basin boundary has a rather complicated structure, as figs 5(b) and 5(c) show, and the numerical studies of this paper indicate that it is indeed a fractal set. This magnification, however, reveals a fractal character quite different from that exhibited by the boundary of the analytic map; here, the boundary appears "stretched" or "striated" in contrast to the "snowflake" appearance of fig. 4. For the class of two-dimensional maps that we study, basin boundaries can be either smooth or fractal. When they are fractal, they almost always exhibit a "stretched" structure similar to fig. 5.

In section 6 we discuss the measure generated by inverse orbits on the basin boundary, the Lyapunov numbers for this measure, and the dimension of the measure. Section 7 concludes the paper with a summary of our main results.

2. Final state sensitivity

Even in the absence of a detailed description of the dynamics of the systems shown in figs. 1–5, one can readily understand the effect that initial condition error has on the ability to predict which final state will be approached by a particular trajectory. If an initial condition specified with error ε is within that distance of the basin boundary, the attractor to which it will be attracted cannot be predicted with certainty. In the

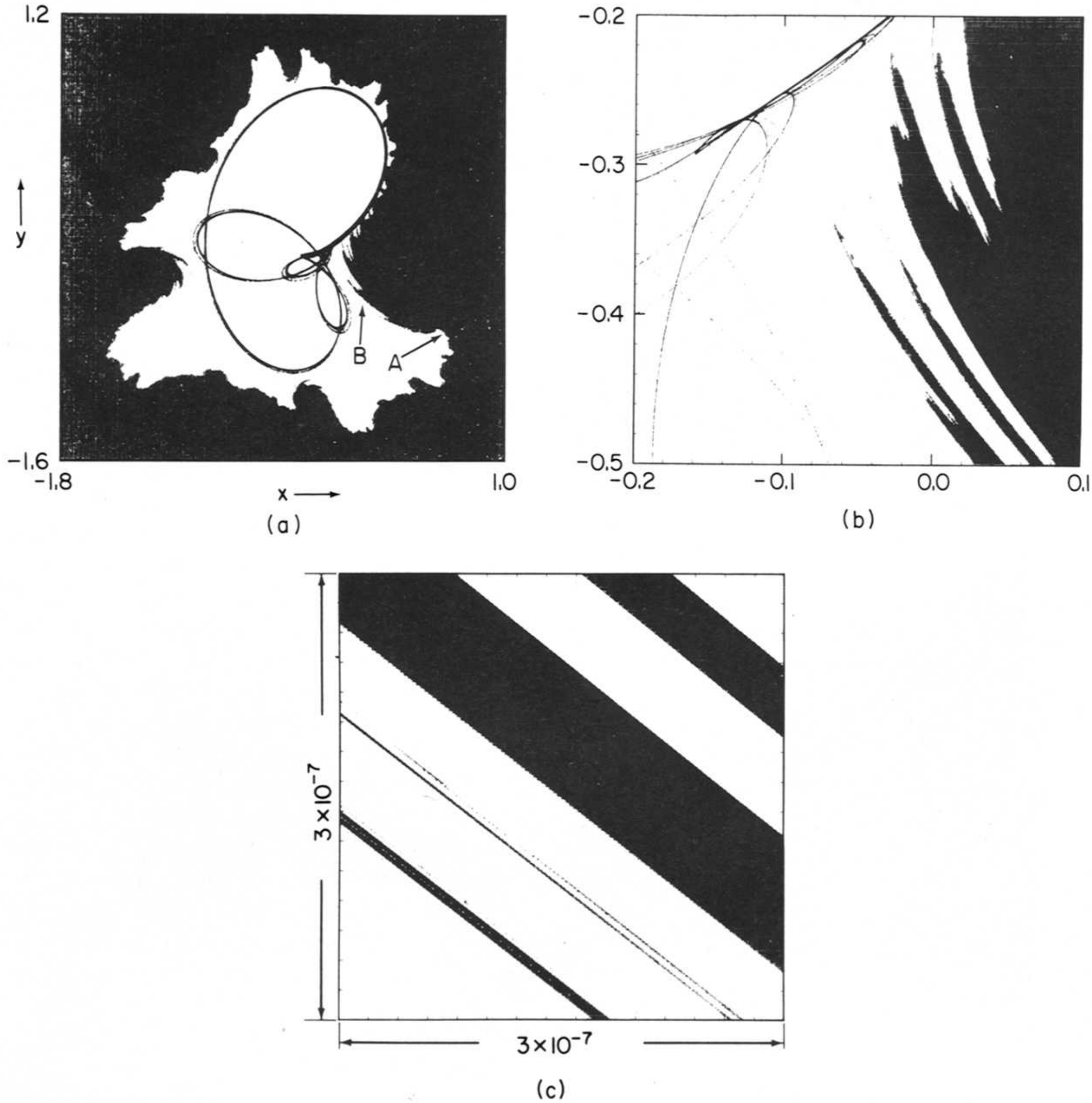

Fig. 5. (a) Basin structure of the mapping given in eqs. (5.15). The chaotic attractor attracts all initial conditions in the blank region while the dark region is the basin for orbits which escape to infinity. An unstable fixed point is located on the basin boundary at A. (b) Magnification of a region near B in (a). (c) Magnification to a scale of 10^{-7} of the region $-0.5316359 \leq x \leq -0.5316356$, $-1.1584159 \leq y \leq -1.1584156$ showing locally striated structure of the boundary.

present section we shall develop this notion of *final state sensitivity* in terms of the fraction of phase space consisting of initial conditions which are uncertain (in the above sense) when specified with error ε. We focus not on the actual size of the uncertain fraction of phase space, but rather on the way in which this fraction scales as the initial condition error is reduced. Furthermore, since the location and structure of a basin boundary depends on the system parameters, uncertainty in system parameter values could affect the ability to predict the final state from an initial condition, independent of the degree of precision with which the initial condition is chosen. Therefore, we shall also investigate parameter sensitivity: the scaling of the uncertain fraction of parameter space with variation in the parameter error, when the initial condition is fixed.

2.1. *Initial condition uncertainty*

In the schematic example shown in fig. 2 with two attractors (A and B) and a simple smooth one-dimensional basin boundary separating the finite volume of phase space, the uncertain region for initial conditions with error ε is simply determined by thickening the basin boundary by the amount ε. Any initial condition in this strip can change from the basin of A to that of B (or vice versa) if perturbed by an amount ε or less. The area of this region is proportional to the error ε; as ε is reduced, the "uncertain fraction" of phase space satisfies

$$f(\varepsilon) \sim \varepsilon. \tag{2.1}$$

For $f(\varepsilon)$ to be well defined in cases where the phase space of the system is infinite, we shall restrict initial conditions to lie in some fixed finite subregion of phase space which contains the basin boundary (e.g., the region pictured in fig. 3a). In such a case, the actual magnitude of $f(\varepsilon)$ at a particular value of ε will depend on the choice of subregion. We are primarily interested in the scaling of $f(\varepsilon)$ as ε becomes small (e.g., eq. (2.1)), however, and we believe that this behavior is independent of the subregion selected. (More precisely, the exponent α in eq. (1.1) is independent of the subregion.)

We now consider the phase space region shown in fig. 3 and examine the dependence of the "uncertain fraction" of phase space $f(\varepsilon)$ on the error ε. This is accomplished by selecting 8192 random initial conditions over the region of fig. 3a and iterating each to determine its final state (i.e., to ascertain the basin in which each is located). Each initial condition (θ_0, x_0) is then perturbed in the horizontal direction by $\pm\varepsilon$ to produce two perturbed initial conditions $(\theta_0 \pm \varepsilon,\ x_0)$. All 16,384 perturbed initial conditions are iterated to determine their basins, and this data is compared to that for the unperturbed initial conditions. If either of the two perturbed initial conditions associated with a particular unperturbed initial condition is in a basin different from the unperturbed one, we say that the initial condition is uncertain under the error ε. We record the fraction $\bar{f}(\varepsilon)$ of these initial conditions as the error ε is varied: we expect this fraction of uncertain initial conditions to be proportional to the uncertain fraction $f(\varepsilon)$ of phase space volume. See subsection 2.3 for further discussion of this.

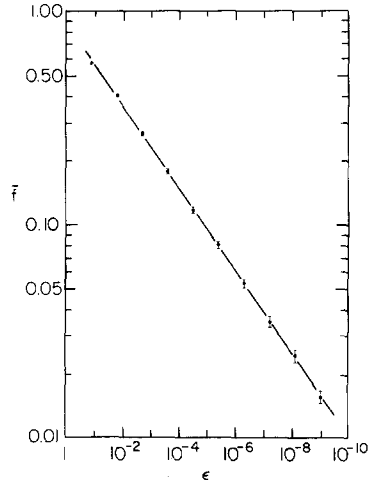

Fig. 6. Log–log plot of $\bar{f}$ versus ε for the phase space shown in fig. 3.

The variation of $\bar{f}(\varepsilon)$ for this system with decreasing error ε is plotted in fig. 6. The error bars at each data point were computed on the basis that occurrences of uncertain initial conditions are random events, and hence the error in their number $N(\varepsilon)$ at a particular value of ε is $\sqrt{N(\varepsilon)}$. Here, the log–log plot indicates a power law behavior with exponent 0.2,

$$\bar{f}(\varepsilon) \approx 0.9\varepsilon^{0.2}. \tag{2.2}$$

The consequences of such a relationship are remarkable. For an error of 0.125 in the initial conditions (about 3% of the width of the phase space shown in fig. 3a), the final states of approximately 59% of the initial conditions could not be predicted with certainty. Reducing the error by about a factor of 60 to 0.002 results in a decrease of $\bar{f}$ to 26%, only about a factor of two increase in one's confidence in the ability to predict.

We expect such a power law behavior,

$$f(\varepsilon) \sim \varepsilon^{\alpha}, \tag{2.3}$$

to be common in dissipative dynamical systems. The uncertainty exponent α is related to the dimension of the basin boundary,

$$\alpha = D - d. \tag{2.4}$$

Here, D is the dimension of the phase space and d is the dimension of the basin boundary. We use the capacity definition of dimension [12]

$$d = \lim_{\delta \to 0} \frac{\ln N(\delta)}{\ln(1/\delta)}, \tag{2.5}$$

where $N(\delta)$ is the minimum number of D-dimensional cubes of side δ required to completely cover the basin boundary. This definition simply expresses the scaling of $N(\delta)$ with the cube size as δ is decreased; for example, we see that the power law

$$N(\delta) \sim \delta^{-d} \tag{2.6}$$

satisfies (2.5). That (2.3) and (2.4) result from (2.5) can be seen heuristically as follows: setting the cube edge δ equal to the initial condition error ε, the volume of the uncertain region of phase space will be of the order of the total volume of all $N(\varepsilon)$ D-dimensional cubes of side ε required to cover the boundary. Since the volume of one of these cubes is ε^D, this uncertain volume is of the order $\varepsilon^D N(\varepsilon)$. With (2.6) for $N(\varepsilon)$, we estimate the uncertain phase space volume to be of the order of $\varepsilon^D N(\varepsilon) \sim \varepsilon^{D-d}$, which gives (2.3) and (2.4). A more precise statement is given by the following rigorous result.

Theorem. The uncertain fraction f of a finite region of a D-dimensional phase space associated with initial condition error ε obeys

$$\lim_{\varepsilon \to 0} \frac{\ln f(\varepsilon)}{\ln \varepsilon} = \alpha, \tag{2.7}$$

if and only if the basin boundary has capacity dimension $d = D - \alpha$.

A proof of this theorem is provided at the end of this section.

The expression (2.3) reduces to the linear relation (2.1) in cases where the basin boundary is a smooth curve or surface so that its dimension is one less than that of the phase space, $d = D - 1$. In general, since the basin boundary divides the phase space, its dimension d must satisfy $d \geq D - 1$. Thus, the existence of fractional dimension boundaries allows for values $0 < \alpha \leq 1$. From (2.4), one concludes that the result (2.2) for the mapping in fig. 3 indicates an experimentally measured fractal basin boundary dimension of approximately 1.8. For the analytic mapping shown in fig. 4 and discussed in section 5.1, the experimental measurement of $\bar{f}(\varepsilon)$ as described above again yields the relationship (2.3) with a value of $\alpha \approx 0.69$; by (2.4), this indicates a basin boundary dimension of about 1.3. The more general quadratic map in fig. 5 produces a similar value $\alpha \approx 0.7$ for a similar dimension of about 1.3, despite the quite different appearance of the basin boundary.

2.2. *Parameter sensitivity*

In addition to affecting the specification of an initial condition, error may also be present in the selection of the parameters of a system. A small error in a system parameter might alter the location or structure of a basin boundary so that a fixed initial condition shifts from one basin to another. In a finite region of parameter space, the fraction of parameter values which will produce such a shift for a given initial condition when perturbed by a parameter error δ is the uncertain fraction $f_p(\delta)$ of parameter space. Here we investigate the scaling of $f_p(\delta)$ at small δ for the map shown in fig. 3. As discussed in section 4.1,

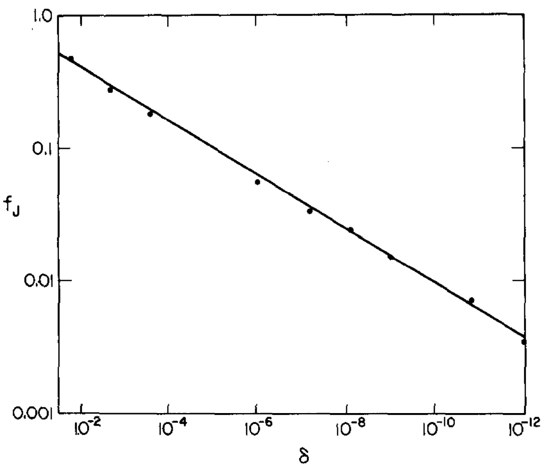

Fig. 7. Log–log plot of f_J versus parameter error δ for the phase space of fig. 3 (eqs. (4.1)).

the parameter we shall vary in this system is denoted J_0 (cf. eqs. (4.1)).

We consider the sensitivity of the basin boundary to variations of the system parameter J_0. We select a single initial condition $(\theta_0, x_0) = (1.05, 0.3)$ with a random choice of J_0 in the interval $0.1 \leq J_0 \leq 0.3$ and determine which attractor ($A^{\pm}$) is approached by this orbit. Then J_0 is perturbed to $J_0 \pm \delta$ and the same initial condition is iterated for both perturbed maps. If either of the parameter perturbations has shifted the basin boundary so that the fixed initial condition has changed from the original basin to the other, we say that this particular unperturbed choice of J_0 is uncertain under the error δ. This experiment is repeated for 12,800 random choices of J_0 in the same interval (all with the same single initial condition) for values of the parameter error δ between $10^{-3} \geq \delta \geq 10^{-12}$. The fraction $f_J(\delta)$ of the uncertain parameter values (in the sense given above) in the parameter interval is plotted as a function of the parameter error δ in fig. 7.

The result of fig. 7 again indicates a power law relationship between the uncertain fraction of parameter space and the parameter error, $f_J(\delta) \sim \delta^{0.2}$. (While it is possible that the dimension of a basin boundary could vary widely over a parameter range, the dimension of the boundary in this system remains close to 1.8 in the parameter interval examined.)

2.3. *Remarks*

1) While the power law behavior (2.2) of $f(\varepsilon)$ observed for the map in fig. 3 satisfies the limiting relationship (2.7), there are other forms of $f(\varepsilon)$ at small ε that would also yield the same value of α. For example, the behavior $f(\varepsilon) \sim \varepsilon^{\alpha} \ln \varepsilon$ also satisfies (2.7). Indeed, an example given in the appendix shows that one can have a smooth basin boundary ($\alpha = 1$) with $f(\varepsilon) \sim \varepsilon \ln(1/\varepsilon)$ for small ε.

2) Imagine that we attempt to initialize the system at a point η in the region of interest (e.g., the rectangle of fig. 3a). If η has an uncertainty ε, then the actual initial condition is $\bar{\eta} = \eta + \varepsilon\Delta$, where $\varepsilon\Delta$ is a random number representing the error. The quantity Δ might be thought of as being generated from some probability density $p(\Delta)$. For example, without loss of generality p can be chosen so that $\int \Delta^2 p(\Delta)\, \mathrm{d}^D\Delta \equiv 1$, in which case ε is the variance of the error $\varepsilon\Delta$. Now choose η randomly in the region of interest and use η to determine the attractor to which the system tends. Since the actual initial condition is $\bar{\eta}$ rather than η, the prediction of the final state might in fact be incorrect. Let $\tilde{f}(\varepsilon)$ denote the probability of this error. Note that $\tilde{f}(\varepsilon)$ and $f(\varepsilon)$ are different: $\tilde{f}(\varepsilon)$ is the probability of making an incorrect prediction, while $f(\varepsilon)$ is the probability of *being able* to make an incorrect prediction if $|\Delta| < 1$. The quantity $\tilde{f}(\varepsilon)$ is measurable by performing repeated experiments. For example, our calculated quantity $f(\varepsilon)$ for the numerical experiments of fig. 3a is an approximation to $2\tilde{f}(\varepsilon)$ for the case $\Delta = (\Delta_x, \Delta_y)$, $p(\Delta) = \delta(\Delta_y)[\delta(\Delta_x - 1) + \delta(\Delta_x + 1)]/2$, where here $\delta(\Delta_x)$ is the standard delta-function. The quantity $f(\varepsilon)$ is, however, in principle much harder to approximate in a numerical experiment.

Pelikan [13] has proven that $\tilde{f}(\varepsilon) \sim f(\varepsilon)$ under the following restrictions: (i) p = constant in $|\Delta| < 1$ and zero otherwise; and (ii) the map is strictly expanding on the basin boundary. The restriction (ii), for example, applies to certain one-dimensional maps and to Julia sets (e.g., fig. 4), but not to our example in fig. 3. In the general case, we believe that the following statement should hold.

Conjecture. For typical dynamical systems

$$\lim_{\varepsilon\to 0}\frac{\ln \tilde{f}(\varepsilon)}{\ln f(\varepsilon)}=1.$$

2.4. *Proof of theorem* (2.7)

Let $B(\varepsilon, A)$ be the set of points within ε of a closed bounded set A and assume A has capacity dimension d. Cover phase space with a cubic grid with cube edge length ε. Each point x of A is in a box of the grid. Any point y within ε of A lies within ε of some point x in A. Therefore y lies in one of 3^D boxes which are the original cube or a cube touching the original cube (see fig. 8). Hence, $B(\varepsilon, A)$ can be covered using no more than $3^D N(\varepsilon)$ cubes where $N(\varepsilon)$ is the number of ε cubes needed to cover A. Thus the volume of the set $B(\varepsilon, A)$ satisfies

$$\mathrm{Vol}(B(\varepsilon, A)) \le 3^D \varepsilon^D N(\varepsilon). \tag{2.8}$$

Now we cover A using cubes from a grid with edge lengths $\varepsilon/D^{1/2}$. We choose that size grid since any two points within such a cube are within ε of each other. Thus every point in every cube used in the cover is within ε of A, and so lies in $B(\varepsilon, A)$. Such a cover has $N(\varepsilon/D^{1/2})$ cubes, so

$$\mathrm{Vol}(B(\varepsilon, A)) \ge (\varepsilon/D^{1/2})^D N(\varepsilon/D^{1/2}). \tag{2.9}$$

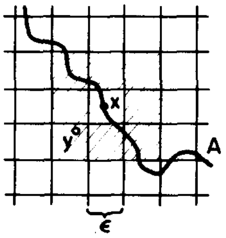

Fig. 8. Schematic representation of a basin boundary set A in a phase space covered with cubes of edge ε.

Thus,

$$\begin{aligned}&\frac{\ln D^{-D/2}}{\ln \varepsilon}+\frac{\ln N(\varepsilon/D^{1/2})}{\ln \varepsilon}+D\\ &\le \frac{\ln[\mathrm{Vol}(B(\varepsilon, A))]}{\ln \varepsilon}\\ &\le \frac{\ln 3^D}{\ln \varepsilon}+\frac{\ln N(\varepsilon)}{\ln \varepsilon}+D.\end{aligned}$$

From the definition of d, eq. (2.5),

$$\lim_{\varepsilon\to 0}\frac{\ln[\mathrm{Vol}(B(\varepsilon, A))]}{\ln \varepsilon}=D-d.$$

Let A be the portion of the basin boundary in the region of interest (as in the rectangle of fig. 3a). Since $f(\varepsilon)$ is proportional to $\mathrm{Vol}(B(\varepsilon, A))$, eq. (2.7) follows.

3. Classification of fractal basin boundaries

3.1. *Classification*

In figs. 3, 4, and 5 of section 1 we have given several examples of fractal basin boundaries. The boundaries in these figures appear to have quite different structure, and indeed the types of basin boundaries which they exemplify are fundamentally different. In this section we offer a classification of fractal basin boundaries, ordered below in terms of increasing degree of regularity of the boundary:

(i) boundaries which are *locally disconnected* (e.g., fig. 3);

(ii) boundaries which are *locally connected* but are not quasicircles (e.g., fig. 5);

(iii) boundaries which are *quasicircles* (e.g., fig. 4).

3.2. *Definitions*

A closed set is *disconnected* if it can be split into two parts A and B such that

$\min|\alpha-\beta|>0$

for α in A and β in B. If this cannot be done then the set is *connected*.

A set is *locally connected* if, given any point η in the set and any sufficiently small ε, then there exists a $\delta(\varepsilon, \eta) \leq \varepsilon$ with the following property:

P) For every point ξ in the set satisfying $|\eta - \xi| \leq \delta(\varepsilon, \eta)$, there is a connected subset of the original set containing η and ξ and lying wholly in the ε-ball centered at η.

If the property P is not satisfied for every η in the set, then we say that the boundary is *locally disconnected.*

If the property P can be satisfied with $\delta = \kappa\varepsilon$ for some constant κ independent of η, then the set is a *quasicircle.*

From our definition, it follows that the boundary is locally connected if it is a continuous curve or surface. A continuous surface lying in a D-dimensional phase space is a surface which is parametrically representable as $x = g(s)$, where s is a D-1-dimensional parameter vector, x is a point on the boundary, and g is a continuous D-dimensional vector function of s.

If the basin boundary is locally connected and bounded, then one can show that $\delta(\varepsilon, \eta)$ can be chosen independent of η, $\delta(\varepsilon, \eta) = \delta(\varepsilon)$.

3.3. *Examples*

In order to give the reader a feel for these definitions we list below several illustrative examples applying these definitions.

Example 1. A simple smooth curve such as the basin boundary pictured in fig. 1 is connected (but not fractal).

Example 2. The logistic map, $x_{n+1} = rx_n(1 - x_n)$, has two attractors for $0 < r < 4$. One of these attractors is $x = -\infty$. The other is located in the region $1 > x > 0$ and may be either periodic or chaotic depending on r. The basin boundary for these two attractors are the two points $x = 0$ and $x = 1$. To apply the definition, identify η in the definition with one of these two points, say $x = 0$, and take $\varepsilon < 1$. Then $\xi = \eta = 0$, and property P is clearly satisfied. The boundary is locally connected.

Example 3. In section 5 we shall consider a mapping of a cylinder for which the basin boundary can be determined analytically and is given by

$$y = B(x) = -\sum_{j=1}^{\infty} \lambda_y^{-j} \cos\left(2\pi\lambda_x^{j-1}x\right), \tag{3.1}$$

where λ_x is an integer, $\lambda_x > \lambda_y > 1$ and $-1 < x < 1$. This basin boundary is shown in fig. 19. The sum (3.1) converges absolutely and uniformly for $\lambda_y > 1$ so that $B(x)$ is a continuous curve; therefore, the basin boundary is locally connected. As such, (3.1) can be formally differentiated term by term,

$$\frac{\mathrm{d}B}{\mathrm{d}x} = \frac{2\pi}{\lambda_x} \sum_{j=1}^{\infty} \left(\frac{\lambda_x}{\lambda_y}\right)^j \sin\left(2\pi\lambda_x^{j-1}x\right). \tag{3.2}$$

Since $\lambda_x > \lambda_y > 1$, we see that (3.2) diverges. Thus, the boundary $y = B(x)$ is a continuous but nowhere differentiable curve. Furthermore, the boundary has infinite length and can be shown [14] to have capacity dimension $d = 2 - (\ln\lambda_y / \ln\lambda_x)$.

We now show heuristically that this basin boundary is not a quasicircle. Let us focus on the behavior of (3.1) near $x = 0$, where $B(x)$ is schematically depicted in fig. 9. As prescribed in the definition of local connectedness, we select the point $\eta \equiv (x_*, B(x_*))$ on the boundary to be the center of an ε-ball. In order to apply the property P, we ask the following question: if we construct a ball of radius δ around η (as shown in fig. 9) which includes the boundary point $\xi_* \equiv (-x_*, B(-x_*))$, how large must ε be so that a connected piece of the boundary containing η and ξ_* lies within the ε-ball centered at η? We shall show that as x_* becomes smaller, the required radius ε diminishes as $\delta(\varepsilon) \sim \varepsilon^{\gamma}$, with $\gamma > 1$.

From (3.1) we note that $B(x_*) = B(-x_*)$, so that the distance between ξ_* and η is simply the horizontal displacement $\delta = 2x_*$. Referring to fig. 9, we see that for η and ξ_* to lie on a connected piece of the boundary contained entirely within an ε-ball centered at η, we must choose ε large enough to include the boundary point $m \equiv (0, B(0))$. Therefore, $\varepsilon(x_*) \geq |m - \eta| \approx |B(x_*) - B(0)|$, for $\varepsilon \gg x_*$ (since $\delta \sim \varepsilon^{\gamma}$, $\gamma > 1$, and x_* is small). Now we note that (3.1) implies $B(x/\lambda_x) = \lambda_y^{-1}[B(x) - \cos(2\pi x/\lambda_x)]$, so that $B(0) = \lambda_y^{-1}[B(0) - 1]$. Com-

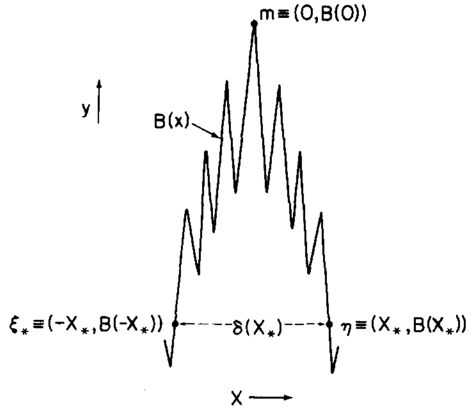

Fig. 9. Schematic representation of the basin boundary $B(x)$ of fig. 19 near $x = 0$. Choosing the point η on the boundary, the radius of an ε-ball around η must be $\varepsilon = |m - \eta|$ so as to include a connected piece of $B(x)$ connecting η to the point ξ_* a distance δ away.

bining these two relations, we see that $\varepsilon(x_*/\lambda_x)$ is

$$\begin{aligned}\varepsilon(x_*/\lambda_x) &\approx |B(x_*/\lambda_x) - B(0)| \\ &\approx \lambda_y^{-1}|B(x_*) - B(0) + 1 \\ &\quad - \cos(2\pi x_*/\lambda_x)| \\ &\approx \lambda_y^{-1}|B(x_*) - B(0)| \\ &\approx \varepsilon(x_*)/\lambda_y,\end{aligned}$$

where we have neglected the contribution $1 - \cos(2\pi x_*/\lambda_x)$ for small x_*. Thus we see that as x_* is diminished by a factor of λ_x, the required radius of the ε-ball decreases by a factor of λ_y. Thus, $\varepsilon(x_*) \sim x_*^{1/\gamma}$, with $\gamma = (\ln \lambda_x / \ln \lambda_y) > 1$. Combining this with $\delta(x_*) \sim x_*$, we have

$$\delta(\varepsilon) \leq \mathcal{O}(\varepsilon^\gamma).$$

While we have derived this result by considering a region in the vicinity of $x = 0$, we emphasize that the same behavior must occur near every $x = m/\lambda_x^n$ for all positive integers m and n. Thus, since $\gamma > 1$, to satisfy property P, $\delta(\varepsilon)$ must shrink to zero faster than linearly with ε as $\varepsilon \to 0$; we cannot satisfy property P with $\delta(\varepsilon) = \kappa\varepsilon$. We conclude that (3.1) is an example of a fractal basin boundary that is connected but is not a quasicircle. Due to the similar appearance upon magnification of the basin boundary of fig. 5 and that in fig. 19, we believe that the boundary in fig. 5 is also connected but not a quasicircle (cf. section 5 for further discussion).

Example 4. By definition the largest connected subset of a Cantor set is a single point; yet in any neighborhood of a point in a Cantor set there are an infinite number of other points in the Cantor set. Thus a Cantor set is locally disconnected. In the next section we discuss a one-dimensional map model of the Lorenz system of differential equations; for this map the basin boundary is a Cantor set. In addition, the magnification of the basin boundary shown in fig. 3b is essentially a Cantor set of parallel line segments (see section 4), and thus also is an example of a disconnected basin boundary.

3.4. *Discussion*

In the following section we discuss several dynamical systems with locally disconnected fractal basin boundaries. Following that, section 5 is devoted to a discussion of locally connected basin boundaries. Locally connected basin boundaries arising from an analytic map of a single complex variable, $z \to F(z)$, where $z = x + iy$ and F is analytic, have been studied for a long time. Such maps yield quasicircle basin boundaries [11]. However, such maps are also special, and we believe that the quasicircle property should not be expected to occur in *typical* dynamical systems. To our knowledge, our discussion of section 5 is the first (with the exception of our preliminary note, ref. 4) to address locally connected fractal basin boundaries that are not quasicircles.

From the examples of section 5 it appears that locally connected fractal basin boundaries require a minimum system dimensionality for their existence. In particular, for smooth invertible maps, the dimension must be at least three, corresponding to four for continuous time systems (flows). For smooth noninvertible maps the dimensionality is evidently required to be at least two. In contrast, like chaotic attractors, locally disconnected fractal basin boundaries can occur in smooth one-dimensional noninvertible maps and in smooth two-dimensional invertible maps.

4. Locally disconnected basin boundaries

The development of the present understanding of chaotic motion in dynamical systems has relied on the investigation of several standard physical models. In particular, the behavior of the forced van der Pol oscillator in certain parameter regimes was studied by Cartwright and Littlewood [5] who suggested the presence of chaotic (although nonattracting) orbits as well as an infinity of periodic orbits (also nonattracting). The ensuing work of Levinson [6] on a class of chaotic orbits in this system led to the geometric interpretation of Smale [15] and his introduction of the horseshoe map. This general construction has since influenced the analysis of chaotic behavior in many systems, and its specific application to the van der Pol oscillator is described in the work of Levi [7]. Levi points out, in passing, that the van der Pol system possesses a basin boundary that is a Cantor set and Flaherty and Hoppensteadt [16] comment briefly that Levinson's solutions are orbits on this boundary. However, there is virtually no literature on fractal basin boundaries, and the important practical implications of this type of boundary structure, which we discuss in this paper, have not been studied.

The basin boundary for the case studied in refs. 5–7 and 16 is an example of a locally disconnected fractal basin boundary. In this section we shall give a detailed discussion of several other examples of locally disconnected fractal basin boundaries. The general impression emerging from the discussion of this section is that such boundaries may be commonly encountered in practical situations. We begin in section 4.1 with an examination of the basin boundary (shown in fig. 3) which arises in a model similar to (but simpler than) that used by Levi to describe the qualitative behavior of the van der Pol oscillator. While the van der Pol equation has two attracting orbits of periods n and $n+2$ for some n, our model has two attracting fixed points.

4.1. *A model annulus map*

Consider a map on the annulus $\mathscr{A}$ in the plane as shown in fig. 10. We use polar coordinates (r, θ) with θ measured from the horizontal axis as shown. Phase points in $\mathscr{A}$ at time $t = 0$ are mapped into the thinner convoluted annulus $\mathscr{A}'$ at $t = 1$. Thus we are considering a discrete time map (which might arise via Poincaré surface of section [1] from a continuous time system). The effect of this map M on the region between $\theta = 0$ and $\theta = \pi$ is to squeeze the annulus radially, stretch it in length, and to fold the region near $\theta = \pm\pi/2$ as shown. The points $A^{\pm}$ at $\theta = 0, \pi$ are attracting fixed points of the map. The map M is taken to be symmetric under reflection across the horizontal axis $(\theta \to 2\pi - \theta)$. An explicit map with these properties will be given later.

The angular aspect of the two-dimensional map M may be simulated by the one-dimensional map $M_1(\theta)$ which is shown in fig. 11. In addition to the stable fixed points $A^{\pm}$ at $\theta = 0, \pi$, there are three unstable fixed points: S_+ at $\theta = \theta_+$, S_- at $\theta = \theta_-$, and S_0 at $\theta = \pi/2$. In the full two-dimensional geometry of the annulus, these points are located at the crosses in fig. 10; they are within the image annulus $\mathscr{A}'$ and continue to be within all successive images of the original annulus $\mathscr{A}$. Thus, $S_{\pm}$

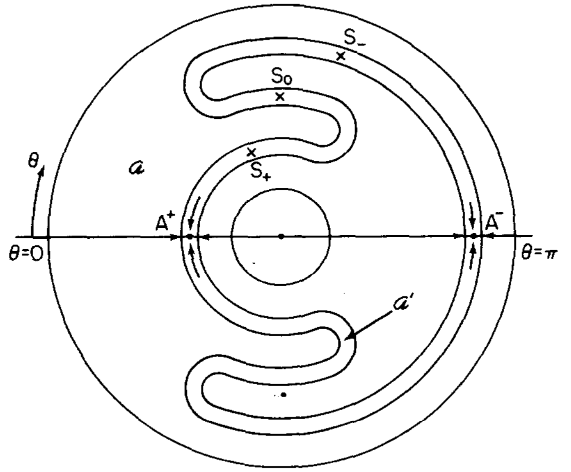

Fig. 10. The mapping M maps the annulus $\mathscr{A}$ to the thinner convoluted annulus $\mathscr{A}'$ such that there are two attracting fixed points $A^{\pm}$ and saddle points S_+, S_-, and S_0.

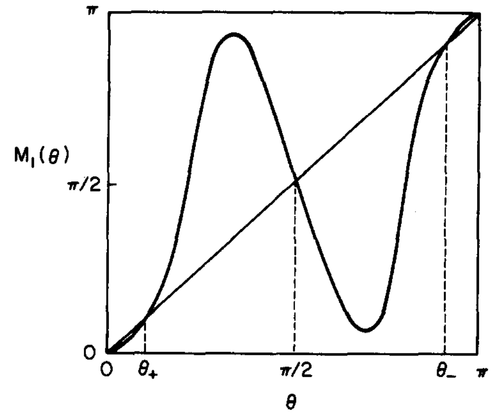

Fig. 11. The angular behavior $M_1(\theta)$ of the annulus map M of fig. 10.

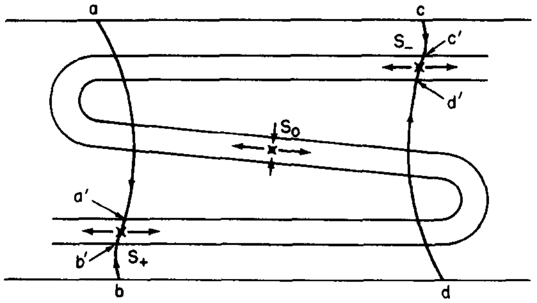

Fig. 12. Schematic illustration of the convolution of $\mathscr{A}'$ near $\theta = \pi/2$.

and S_0 are actually saddles due to the radial contraction under M.

The action of M in the convoluted region near $\theta = \pi/2$ is schematically illustrated in fig. 12, where the arc has been straightened out. Here, the saddles $S_\pm$ and S_0 are shown with their local contracting and stretching directions. The extension $\overline{ab}$ of the contracting direction of S_+ is the part of the stable manifold of S_+ which maps to $\overline{a'b'}$ under one iteration of M; similarly, $\overline{cd}$ is the piece of the stable manifold of S_- which maps to $\overline{c'd'}$. Comparing fig. 12 with fig. 10 and in view of the properties of the stable manifolds of S_+ and S_-, all points in the region to the left of $\overline{ab}$ will map toward the attractor A^+; all points to the right of $\overline{cd}$ will tend to A^-. Thus, the region to the left (right) of $\overline{ab}(\overline{cd})$ is a part of the basin of attraction for $A^+(A^-)$. We shall see, however, that the region between $\overline{ab}$ and $\overline{cd}$ contains more pieces of each of these basins in an extremely intermingled order.

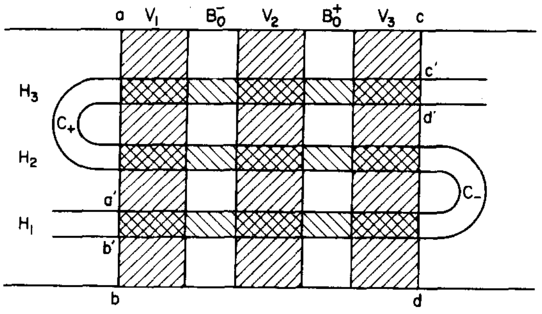

Fig. 13. Further simplification of the region in fig. 12, identifying the action of M on particular subregions of the rectangle abdc: $M(V_i) = H_i$ for $i = 1, 2, 3$, and $M(B_0^\pm) = C_\pm$.

The region of the annulus near $\theta = \pi/2$ in fig. 12 is further schematized in fig. 13, where $\overline{ab}$ and $\overline{cd}$ have been straightened. Again, the action of the map M on the rectangle abdc is to squeeze the region vertically, stretch it out horizontally (to more than triple its original length), and then form the "s" shape with $\overline{ab} \to \overline{a'b'}$ and $\overline{cd} \to \overline{c'd'}$. Thus, the crosshatched region V_1 at the left end of abdc is mapped to the lowest horizontal strip H_1 (also crosshatched). Similarly, V_2 maps to H_2 and V_3 to H_3. The region to the left of $\overline{ab}$ is a piece of the basin of attraction of the attractor A^+; the region to the right of $\overline{cd}$ is a piece of the basin for A^-.

The vertical strip B_0^- between V_1 and V_2 is the preimage of the arc C_- which connects H_1 and H_2; B_0^+ maps to the arc C_+. Since the arc $C_+(C_-)$ is to the left of $\overline{ab}$ (right of $\overline{cd}$), its future iterates tend to the attractor $A^+(A^-)$. Therefore, we see that the vertical strip $B_0^+(B_0^-)$ is a piece of the basin of attraction of $A^+(A^-)$. The basins of the two attractors are now seen to be "tangled", with the regions B_0^+ and B_0^- in "inverted" order (i.e., B_0^+ is closer to A^- than is B_0^-). The future of the three remaining strips (V_1, V_2, and V_3) is as yet undetermined; we define the union of these strips to be the set $\beta_1 \equiv V_1 \cup V_2 \cup V_3$.

We now consider the future of the horizontal strip $H_1 = M(V_1)$. The segment $H_1 \cap B_0^- \equiv H_1^-$ will eventually tend to the attractor A^- since it is in the basin of attraction for A^-. Similarly, the segment $H_1 \cap B_0^+ \equiv H_1^+$ will tend to A^+. As H_1 is the image of V_1 with $\overline{ab} \to \overline{a'b'}$, one may now subdivide V_1 into thinner vertical strips: these are the preimages of $\mathrm{H}_\mathrm{I}^\pm$ and the remaining three sections of H_1, $\mathrm{H}_{1i} \equiv \mathrm{H}_1 \cap \mathrm{V}_i$ $(i = 1,2,3)$. This is shown in fig. 14, where the strip V_1 is partitioned into five thinner strips. The strips V_{1i} map to H_{1i}; these are separated by the strips $\mathrm{B}_\mathrm{I}^\pm$ which map to $\mathrm{H}_\mathrm{I}^\pm$.

Since H_I^+ eventually maps to A^+, its preimage B_I^+ must be a piece of the basin of attraction for A^+. Similarly, B_I^- is a piece of the basin of attraction for A^-. The other two vertical strips, V_1 and V_2, may be similarly partitioned and so contain pieces $\mathrm{B}_i^\pm$ $(i = 2,3)$ of the basin of $\mathrm{A}^\pm$. The alternating order of these pieces indicates an even higher degree of tangling than previously noted. At this stage there are nine vertical strips $\mathrm{V}_{ij}(i, j = 1, 2, 3)$ with undetermined futures. The union of these strips with two indices is defined as the set $\beta_2 \equiv \bigcup_{i,j} \mathrm{V}_{ij}$.

Indeed, this structure continues when one considers the future $M(\mathrm{V}_{ij})$ of V_{ij}. For illustration, consider $M(\mathrm{V}_{11}) \equiv \mathrm{H}_{11}$. Since $\mathrm{H}_{\mathrm{I}\mathrm{I}}^\pm \equiv \mathrm{H}_{11} \cap \mathrm{B}_\mathrm{I}^\pm$ will eventually map to $\mathrm{A}^\pm$, the vertical strip V_{11} is further divided into the 5 substrips $\mathrm{B}_{\mathrm{I}\mathrm{I}}^\pm$ and V_{11i} such that $\mathrm{H}_{\mathrm{I}\mathrm{I}}^\pm = M(\mathrm{B}_{\mathrm{I}\mathrm{I}}^\pm)$ and $\mathrm{H}_{11i} = M(\mathrm{V}_{11i})(i = 1, 2, 3)$. We see that at the nth stage of this process a vertical strip $\mathrm{V}_{j_1 j_2 \cdots j_n}(j_i = 1, 2, 3)$ can be further identified to contain substrips $B_{j_1 j_2 \cdots j_n}^\pm$, which are pieces of the basins of $\mathrm{A}^\pm$, separated by a new series of substrips $\mathrm{V}_{j_1 j_2 \cdots j_{n+1}}$. At each step n we define the union of the 3^n vertical strips with undetermined future $\mathrm{V}_{j_1 j_2 \cdots j_n}$ to be the set

$$\beta_n \equiv \bigcup_{j_1, j_2, \cdots j_n} \mathrm{V}_{j_1, j_2, \cdots j_n}.$$

This process of division is similar to that found in the standard horseshoe construction [17] and produces a Cantor set. As $n \to \infty$, the basin boundary β is given by

$$\beta \equiv \lim_{n \to \infty} \bigcap_n \beta_n.$$

Thus the part of the basin boundary lying in the rectangle abcd of fig. 13 is the product of a Cantor set (running horizontally) and an interval (running vertically). Hence the boundary is locally disconnected (cf., example 4 of section 3.3).

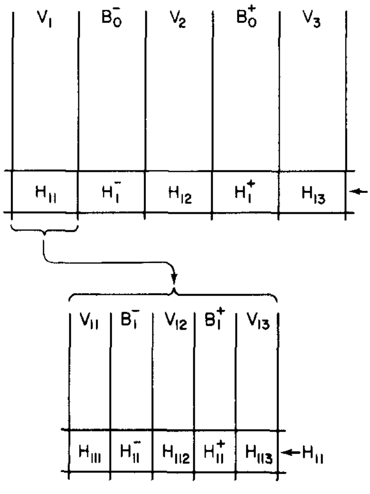

Fig. 14. Simplifying fig. 13, the top picture shows only the vertical strips and the lowest horizontal strip $\mathrm{H}_1 = M(\mathrm{V}_1)$. The bottom picture shows the partitioning of V_1 into the five substrips which are preimages of the five pieces of H_1: $M(\mathrm{V}_{1i}) = \mathrm{H}_{1i}$ for $i = 1, 2, 3$ and $M(\mathrm{B}_\mathrm{I}^\pm) = \mathrm{H}_\mathrm{I}^\pm$. Also identified are the pieces involved in the next level of the construction: the intersections of the substrips of V_1 with H_{11}.

We now give a specific example of a map which has the essential geometric properties outlined above,

$$\theta_{n+1} = \theta_n + a\sin 2\theta_n - b\sin 4\theta_n - x_n \sin\theta_n, \quad (4.1\mathrm{a})$$

$$x_{n+1} = -J_0 \cos\theta_n, \quad (4.1\mathrm{b})$$

where x may be thought of as the radial distance from the center of the annulus. The angles θ and $\theta + 2\pi$ are identified as equivalent and the desired reflection symmetry for $\theta \to 2\pi - \theta$ is present. At fixed x_n, the graph of θ_{n+1} versus θ_n is similar to that in fig. 11 and is adjustable with the two parameters a and b. The x-dependent part of (4.1a) and the form of (4.1b) were chosen in a simple way so that the map is everywhere contracting for $J_0 < 1$ (the Jacobian determinant is $J_0 \sin^2\theta$).

Like fig. 10, this map has two fixed points $\mathrm{A}^+ = (\theta_+, x_+) = (0, -J_0)$ and $\mathrm{A}^- = (\theta_-, x_-) = (\pi, J_0)$ which are attracting for values of a, b, and J_0 such that $|1 + 2a - 4b + J_0| < 1$. The parameters must also be adjusted for these two fixed points to be the only attractors present. Our choice of $a = 1.32$, $b = 0.9$, and $J_0 = 0.3$ seems to satisfy these requirements.

We have examined the basin structure of (4.1) with the stated choice of parameters by considering a grid of 256×256 initial conditions over the region $0 \leq \theta \leq \pi$ and $-0.5 \leq x \leq 0.5$. Each initial condition was iterated 100 times, which is long enough to ensure that all these orbits come within a distance of 10^{-3} from one of the two attractors. The basins for A^+ and A^- are shown in fig. 3, which was constructed by placing a dot at the location of each initial condition whose trajectory approached A^+ at $(0, -0.3)$. The solid vertical dark region to the left of $\theta \approx 0.3$ corresponds to the region to the left of $\overline{ab}$ in fig. 13; the blank region between $2.8 \leq \theta \leq \pi$ corresponds to the region to the right of $\overline{cd}$. This correspondence with figs. 13 and 14 can be continued: the blank parabolic strip at $0.8 \leq \theta \leq 1.4$ is B_0^-, the inverted dark parabolic region at $1.8 \leq \theta \leq 2.4$ is B_0^+, the blank strip at $\theta \approx 0.5$ is B_1^- and the somewhat thinner dark strip a $\theta \approx 0.7$ is B_1^+, etc. The slight tilt of the strips and the parabolic shapes are due to the x-dependence of the map which was, for the most part, ignored in the schematic figs. 12 and 13.

The richness of this basin structure is further revealed upon magnification of the small region $1.92200 \leq \theta \leq 1.92201$, $-0.50000 \leq x \leq -0.49999$ (a scale of 10^{-5}) as shown in fig. 3b. The basins are evidently intertwined to an extreme degree and the fractal Cantor set nature of the basin boundary is indicated.

4.2. *Other examples of locally disconnected boundaries*

The preceding discussion of the existence of basin boundaries which are locally disconnected was illustrated by a two-dimensional mapping (4.1) selected to exhibit the properties of an annulus map developed in figs. 10–14. There are, however, more familiar systems which possess this type of basin boundary structure. There has also been recent experimental evidence implying the existence of fractal basin boundaries in an actual physical system. Here we briefly describe three additional examples in which fractal basin boundaries occur.

1) *The one-dimensional logistic map*

The basin structure of a one-dimensional map with N coexisting attractors sometimes consists of N collections of one-dimensional line segments (basins) separated by a basin boundary composed of a finite set of points. In other examples, the basin boundary is fractal, a Cantor set of fractional dimension. The uncertainty exponent α observed in the power law behavior (1.1) described in section 2 could be used to determine the dimension (2.4) of the basin boundary. An example of a fractal basin boundary is provided by the logistic map, here written in the form

$$x_{n+1} = F_\lambda(x_n) = \lambda - x_n^2, \quad |x| \leq 2. \tag{4.2}$$

In the parameter range $1.75 \lesssim \lambda \lesssim 1.79$, the attractor is a periodic orbit with period three (cf. refs. 10, 18, and 19 for results concerning this regime). In order to construct a one-dimensional map with more than one attractor, we consider the third iterate $F_\lambda^{(3)}$ of (4.2): each element of the period three attractor is a fixed point attractor of $F_\lambda^{(3)}$ with its own basin of attraction. In terms of the original map, each basin is the set of initial conditions which eventually progress around the period three orbit in the same phase. Thus, when considering the original map F_λ we speak of "final phase sensitivity", while for $F_\lambda^{(3)}$ we refer to final state sensitivity as before.

The final state sensitivity experiment was performed as described in section 2 for the third iterate map $F_\lambda^{(3)}$ with $\lambda = 1.75$. The fraction $\bar{f}(\varepsilon)$ of 12,800 initial conditions which changed from one basin to another when perturbed by an error ε is expected to be proportional to the uncertain volume (length) of phase space; the behavior of $\bar{f}(\varepsilon)$ as ε is reduced is shown in fig. 15. Again, a power law behavior $\bar{f}(\varepsilon) \sim \varepsilon^{0.03}$ is evident, with an uncertainty exponent which implies a basin boundary dimension (2.4) of approximately 0.97.

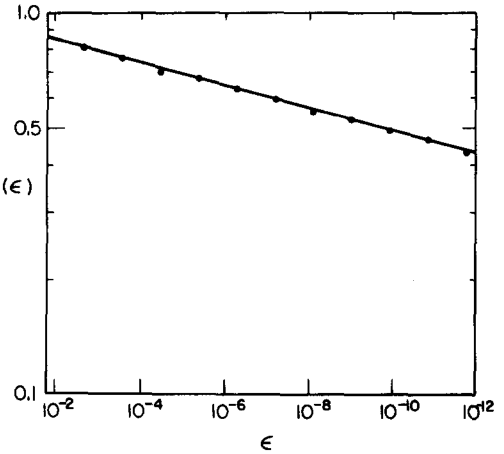

Fig. 15. Log–log plot of $\bar{f}$ versus ε for the third iterate of the logistic map in the period three regime.

2) *Lorenz system*

The Lorenz system [9] of three ordinary differential equations (a truncated model of fluid convection) progresses through several regimes of motion as a parameter r is increased. For values of r in the range $0 < r < 1$, there is a single fixed point attractor at the origin of the three-dimensional phase space representing a stationary fluid without flow. As r is increased through unity, this fixed point becomes unstable and two separate fixed point attractors appear (representing left- and right-handed convective rolls); these are stable in the regime $1 < r < r_c$. A strange attractor appears at a parameter value r_* slightly less than r_c; in this parameter range $r_* < r < r_c$, the two fixed point attractors coexist with the strange attractor. Increasing r through the critical value r_c brings the instability of the two fixed points, and for $r > r_c$ the only attractor is the strange attractor. We concentrate on the parameter range $r < r_*$ in which there are only the two coexisting fixed point attractors.

We consider the three-dimensional phase space in rectangular coordinates. The two fixed point attractors A and B lie in a plane P defined by $z = r - 1$ (in Lorenz's notation) as shown in fig. 16a. We follow Kaplan and Yorke [8] and consider the mapping ϕ on P induced by the repeated downward ($\dot{z} < 0$) intersections of a trajectory in the three-dimensional space with this plane.

In the parameter range $1 < r < r_*$, the origin (0,0,0) is an unstable fixed point possessing a two-dimensional stable manifold S_0 and a one-dimensional unstable manifold U_0. The curve L in

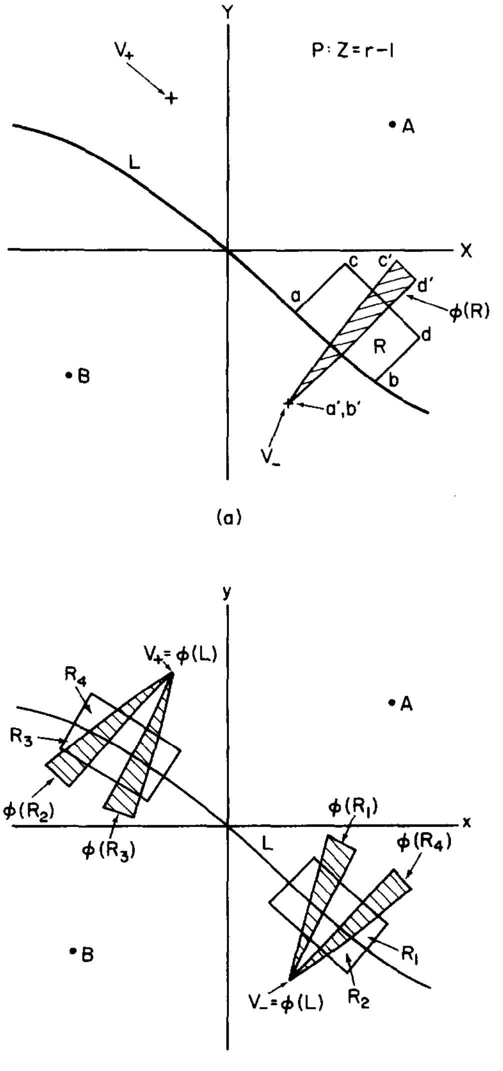

Fig. 16. (a) The flow of the Lorenz system in a three-dimensional phase space induces the mapping ϕ on the plane P (defined as constant z). This qualitative illustration of ϕ shows how points in a region R on P near the stable manifold L map across L and converge near the unstable manifold V_-. (b) More complete illustration of the action of ϕ on regions R_i near L (on both sides).

fig. 16a represents the first intersection of the stable manifold S_0 with P. The points $V_\pm$ are the first downward intersections of U_0 with P, following U_0 in both directions from the origin. Thus, ϕ is not defined on L, and ϕ is discontinuous at L.

Numerical investigation of the orbits for r slightly less than r_* reveal the nature of ϕ, as illustrated in fig. 16a by $R \to \phi(R)$. In general, points far from L on either side uniformly approach the attractor (A or B) on the same side (cd → c′d′). A region near L, however, will map to the other side of L when r is sufficiently close to r_* (abdc → a′b′d′c′). This characteristic of the map is due to a corresponding feature of the flow in this regime: orbits starting near L on P are drawn down toward the origin and then are pushed out and travel near the unstable manifold U_0, crossing over [8] the curve L on the next downward return to the plane P, intersecting P near V_+ or V_-. The schematic triangular shape of the region $\phi(R)$ results from the fact that the closer points in R are to the curve L, the more they tend to be mapped to the same point in $\phi(R)$ (ab → a′b′). The area of $\phi(R)$ is also much smaller than that of R due to the strong contraction experienced by the flow for the standard parameters of the Lorenz system.

The flow admits inversion symmetry in the plane P so that, following Kaplan and Yorke [8], we show in fig. 16b a more complete (yet qualitative) picture of the mapping ϕ near L. Here, the boundaries of the regions R_i $(i = 1,\dots,4)$ which coincide with L map to the pointed tips of the thin triangles shown in fig. 16b. This picture of ϕ, called a "broken horseshoe" in ref. 8, can be used to show that the boundary separating the basins of attraction of A and B is a Cantor set.

As in the previous development in section 4.1, figs. 12–14, of a Cantor set boundary, we redraw fig. 16b as a "reduced broken horseshoe" in fig. 17. That is, we imagine trimming the area of the upper portion of R_1 until the upper boundary of $\phi(R_1)$ coincides with the upper boundary of R_1. Similarly, we trim $R_{2,3,4}$ until we obtain fig. 17a. Comparison of this picture with that of fig. 16b reveals that the crosshatched regions of $\phi(R_1)$ and $\phi(R_4)$ shown in fig. 17a will map to some region between the segment $\overline{p_1p_2}$ of R_3 and the attractor B. Thus, under successive applications of ϕ, these two crosshatched regions will approach B; the same argument implies that the crosshatched pieces of $\phi(R_2)$ and $\phi(R_3)$ (c.f. fig. 17a) will eventually converge to A. This allows us to identify the subregions R_1^B and R_4^B of R_1 and R_4 which are in the basin of B and the subregions R_2^A and R_3^A of R_2 and R_3 which are in the basin of A. These regions are shown as the hatched and shaded strips in the even more schematic fig. 17b. The basin structure in the blank strips of R_1 through R_4 is as yet undetermined.

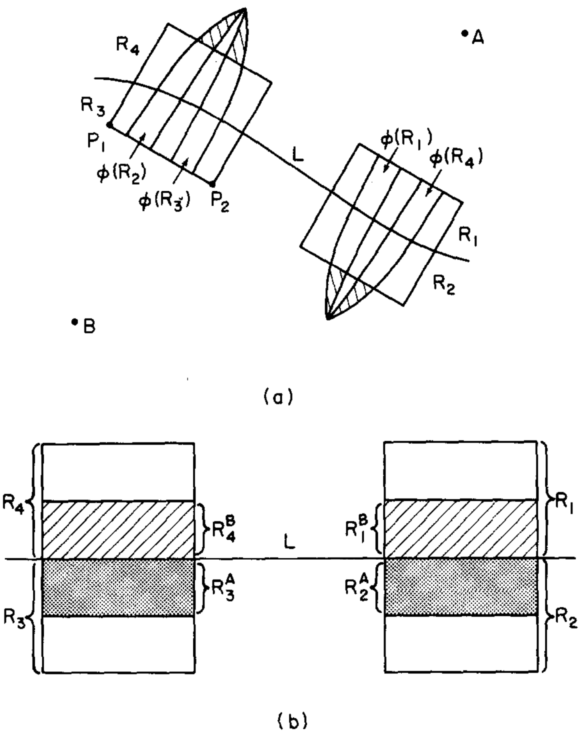

Fig. 17. (a) Reduced broken horseshoe of the map ϕ. The cross-hatched portions of $\phi(R_1)$ and $\phi(R_4)$ will eventually map to attractor B (if R_2 was extended further from L, the image of that portion of R_2 would map to between $\overline{p_1p_2}$ and attractor B (cf. $\phi(R_2)$). (b) Simplified illustration of the regions R_i, showing only the subregions which map to the cross-hatched regions of $\phi(R_i)$ in (a). For example, R_1^B maps to the pointed tip of $\phi(R_1)$ and thence toward B; R_1^B is a piece of the basin of B.

Fig. 18a shows just the two regions R_1 and R_2, separated by the curve L. The hatched strip R_1^B in

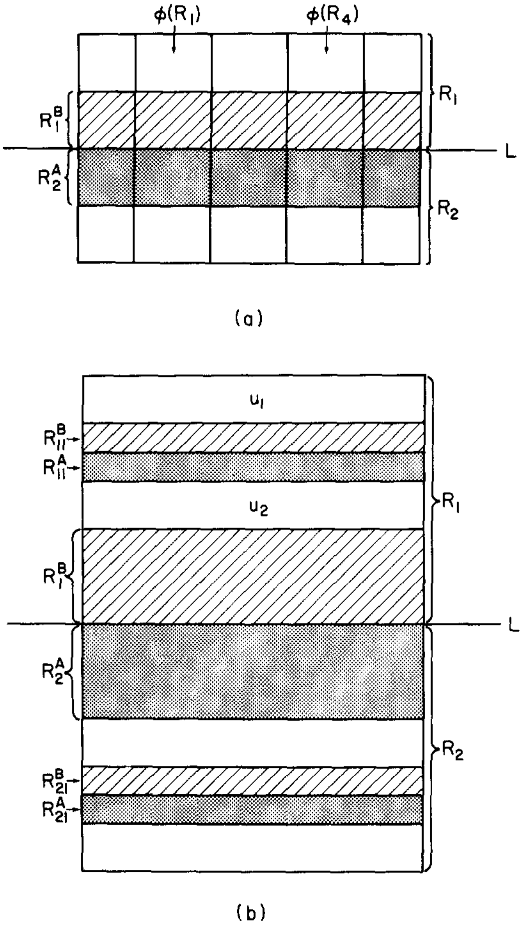

Fig. 18. (a) Illustration of the intersections of R_1 and R_2 with $\phi(R_1)$ and $\phi(R_4)$ (vertical strips, cf. fig. 17a)). (b) Further division of the horizontal blank portions of R_1 and R_2 of (a). The blank region u_1 maps to the blank portion of $\phi(R_1)\cap R_1$, $R_{11}^B \to R_1^B$ (and thence toward B), $R_{11}^A \to R_2^A$ (and thence toward A) and u_2 maps to the blank portion of $\phi(R_1)\cap R_2$. Thus $R_{11}^B(R_{11}^A)$ is in the basin of B(A) and u_1 and u_2 are yet undetermined. Similar arguments apply for the subdivision of R_2.

R_1 has been determined to be a piece of the basin of B, and R_2^A in R_2 is a piece of the basin for A. Now the vertical strips representing the intersection of $\phi(R_1)$ and $\phi(R_4)$ with R_1 and R_2 are also shown. From the definition of R_1^B, we see that points lying in the intersections $\phi(R_1)\cap R_1^B$ and $\phi(R_4)\cap R_1^B$ will eventually approach B, while the region $\phi(R_1)\cap R_2^A$ and $\phi(R_4)\cap R_2^A$ will approach A. Thus, by considering $\phi^{-1}(\phi(R_1))$ we can further deduce that the blank strip of R_1 must at least have the basin structure as shown in fig. 18b. The strip R_{11}^B maps into R_1^B and so is a piece of the basin of attraction for B; similarly, R_{11}^A is a piece of the basin for A. Analysis of the implications of fig. 18a for the region R_4 (due to the intersection of $\phi(R_4)$ with R_1^B and R_2^A) results in a similar partitioning of R_4. Indeed, all four original regions can be analyzed in this manner and can be shown to have the alternating basin structure illustrated in fig. 18b. Furthermore, consideration of the intersections $\phi(R_1)\cap R_{11}^B$ and $\phi(R_1)\cap R_{11}^A$ leads to a similar partitioning of the blank strip u_1; the blank strip u_2 is partitioned by considering $\phi(R_1)\cap R_{21}^B$ and $\phi(R_1)\cap R_{21}^A$. As in the development of section 4.1, this continued process results in a standard horseshoe construction; that is, the remaining undetermined "blank strips" at each stage produce a basin boundary which, in the limit, forms a Cantor set. Almost every point of R_1 and R_2 will eventually approach either A or B, the exceptions being the points on the Cantor set of lines that are mapped into $R_1 \cup R_2$ by all iterates of the map. An indirect effect of the existence of this Cantor set boundary in the parameter regime r slightly less than r_* is provided by the observation of long chaotic transients in numerical investigations, specifically those of Yorke and Yorke [20].

3) *The experiments of Bergé and Dubois* [21]

These authors have performed experiments on the Bénard instability in a low aspect ratio rectangular cell for high Rayleigh number and high Prandtl number. They observe that the system can have multiple attractors, and that a rather long chaotic transient exists before the system settles into one of the attractors. Since the system evolution during the transient phase depends strongly on initial conditions, it is to be expected that the final state will also, and that $\alpha \ll 1$ in (2.3) will apply. At somewhat lower Rayleigh number ($450 \geq r > 200$), different stable attractors still simultaneously coexist but long chaotic transients do not occur. Even in this range it is probable that final state sensitivity will occur.

5. Locally connected basin boundaries

In this section we discuss basin boundaries which are continuous curves or surfaces, but are fractal in that they possess a noninteger capacity dimension and are nowhere differentiable. We shall focus on two-dimensional maps because these systems are relatively simple, computationally rapid to evolve in time, and because they offer a fairly clear visualization of the properties of basin boundaries. We first discuss the tangent map and its Lyapunov numbers.

For a general two-dimensional map M, the tangent map TM (the Jacobian matrix of M) maps infinitesimal displacements $(\delta x_n, \delta y_n)$ near (x_n, y_n) to $(\delta x_{n+1}, \delta y_{n+1})$ near (x_{n+1}, y_{n+1}). We now define the Lyapunov number of an orbit. Consider a forward orbit O^+ given by the sequence $(x_0, y_0; x_1, y_1; \ldots; x_N, y_N)$. By the chain rule for partial differentiation, $\mathrm{TM}^{(N)}(x_0, y_0) = \mathrm{TM}(x_N, y_N) \cdot \mathrm{TM}(x_{N-1}, y_{N-1}) \cdot \cdots \cdot \mathrm{TM}(x_0, y_0)$. Let $l_1^+(N)$ and $l_2^+(N)$ be the eigenvalues of $\mathrm{TM}^{(N)}(x_0, y_0)$, with $|l_1^+| \geq |l_2^+|$. The Lyapunov numbers for the initial condition (x_0, y_0) are

$$\mu_{1,2}^+ \equiv \lim_{N\to\infty} |l_{1,2}^+(N)|^{1/N} \tag{5.1}$$

and the Lyapunov exponents are $h_{1,2}^+ = \ln \mu_{1,2}^+$. In practice, these limits appear to exist and can be estimated easily in numerical computations. In this paper we shall also be interested in Lyapunov numbers for inverse orbits. That is, we start at (x_0, y_0) and consider a sequence of preimages $(x_0, y_0; x_{-1}, y_{-1}; \ldots; x_{-N}, y_{-N})$; we denote this backwards orbit O^-. Infinitesimal displacements $(\delta x_0, \delta y_0)$ near (x_0, y_0) are mapped backwards by the N-composed linear map $\mathrm{TM}^{(-N)}(x_0, y_0) = \mathrm{TM}^{-1}(x_{-N}, y_{-N}) \cdot \mathrm{TM}^{-1}(x_{-N+1}, y_{-N+1}) \cdot \cdots \cdot \mathrm{TM}^{-1}(x_0, y_0)$, where TM^{-1} is the inverse of the matrix TM. Denoting the eigenvalues of $\mathrm{TM}^{(-N)}$ by $l_1^-(N)$ and $l_2^-(N)$, with $|l_1^-| \leq |l_2^-|$, the Lyapunov numbers associated with O^- are

$$\mu_{1,2}^- \equiv \lim_{N\to\infty} |l_{1,2}^-|^{-1/N} \tag{5.2}$$

The backward orbit O^- from (x_0, y_0) is in general not uniquely determined by (x_0, y_0) because the map M may not have a unique inverse. One must remember, therefore, that the backwards Lyapunov numbers $\mu_{1,2}^-$ refer to a particular backwards orbit; a different backwards orbit from (x_0, y_0) may possess a different set of backwards Lyapunov numbers.

5.1. *Analytic maps*

A particular class of two-dimensional maps can be constructed by identifying the plane $\mathbb{R}^2$ with the one-dimensional complex plane $\mathbb{C}^1$ and considering mappings $z_{n+1} = F(z_n)$, where F is an analytic function of the single complex variable $z = x + \mathrm{i}y$. Such a mapping can be resolved to give a two-dimensional map with

$$x_{n+1} = f(x_n, y_n) = \operatorname{Re} F(x_n + \mathrm{i}y_n),$$
$$y_{n+1} = g(x_n, y_n) = \operatorname{Im} F(x_n + \mathrm{i}y_n).$$

For brevity, we refer to two-dimensional maps which satisfy this condition as *analytic maps*. Several properties of these maps greatly facilitate their analysis, and therefore they have been the subject of much study [11]. We emphasize, however, that this is a very special class of two-dimensional maps because the functions $f(x, y)$ and $g(x, y)$ must obey the Cauchy–Riemann conditions in these cases.

The attractors in analytic maps may be fixed points or periodic orbits. A particular analytic map can possess more than one attractor with basins of attraction separated by continuous curves. Despite being continuous, a basin boundary in an analytic map may be nowhere differentiable and may possess a fractal dimension. For our purposes the main facts that we should be aware of concerning analytic maps are (1) they do not exhibit strange attractors; (2) their basin boundaries (Julia sets) are typically fractal curves which exhibit two-dimensional structure on arbitrarily small scales; and (3) their basin boundaries are quasicircles. An example of such a basin boundary is shown in fig. 4.

5.2. *An explicit construction of a locally connected fractal boundary*

In this subsection we consider a two-dimensional map for which an explicit expression for the basin boundary can be derived,

$$x_{n+1} = \lambda_x x_n \quad (\mathrm{mod}\ 1), \tag{5.3a}$$

$$y_{n+1} = \lambda_y y_n + \cos 2\pi x_n, \tag{5.3b}$$

Here λ_x is an integer, x is restricted to the unit interval, but y is allowed to take on all values. The case $\lambda_x = 2$ and $|\lambda_y| < 1$ has been studied by Kaplan and Yorke [22] and has been shown to possess a chaotic attractor which attracts almost all initial conditions. In the following, however, we study the quite different case [4] $\lambda_x > \lambda_y > 1$.

The linearized (or tangent) map

$$\mathrm{TM}(x, y) = \begin{pmatrix} \lambda_x & 0 \\ -2\pi \sin 2\pi x & \lambda_y \end{pmatrix} \tag{5.4}$$

has eigenvalues λ_x and λ_y, which are both greater than one. Thus, since local displacements are always expanded independent of location or initial direction, there are no attractors for this map at finite y. Furthermore, initial conditions with large $|y_0|$ rapidly approach $\pm\infty$ as $\lambda_y^n y_0$, depending on the sign of y. Since no finite attractors exist, we see that the two points at infinity ($y = +\infty$ and $y = -\infty$) are the only attractors.

A picture of the basins for each of these attractors is displayed in fig. 19 for the case $\lambda_x = 3$, $\lambda_y = 1.5$. The dark region is the basin B_- for the attractor at $y = -\infty$ and the blank region is the basin B_+ for $y = +\infty$. The magnification in fig. 19b reveals that linear structure is present on a very small scale; indeed, similar pictures are obtained with repeated magnification of the boundary region. The linear, or "striated" structure on all scales is quite different from the "two-dimensional" or "snowflake" form exhibited by the complex analytic maps of the previous subsection.

We now show that the basin boundary (fig. 19) is a continuous curve of the form $y = B(x)$. In order to proceed, we make use of the fact that since the basin boundary repels trajectories (they all eventually approach $\pm\infty$), it is an attractor for inverse orbits. The map (5.3) is noninvertible;

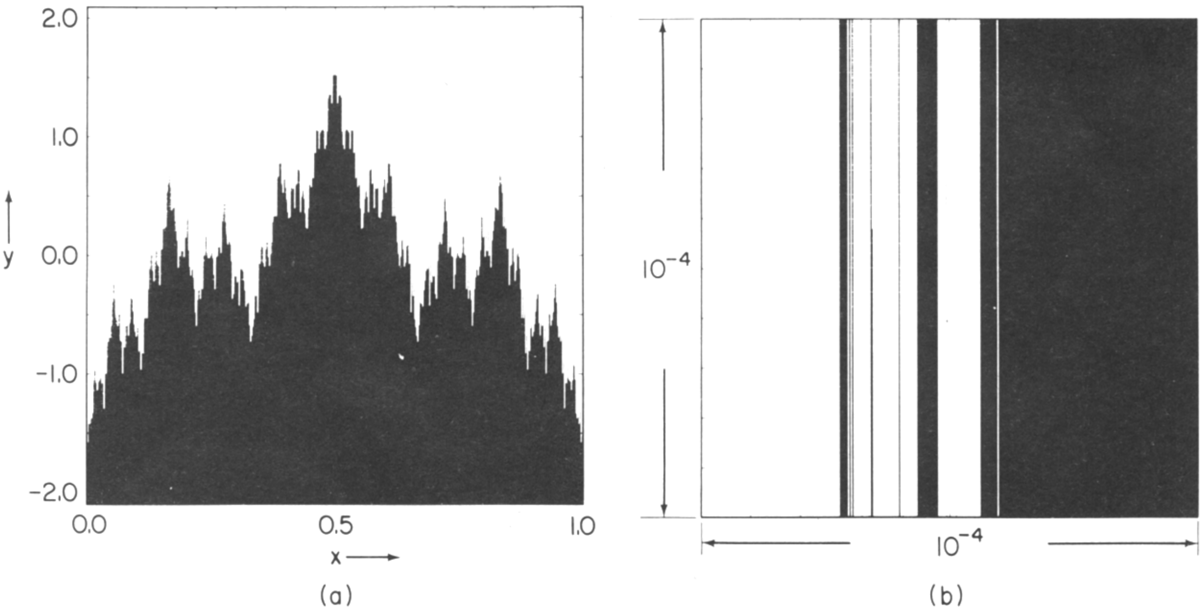

Fig. 19. (a) Basin structure of the system given in eqs. (5.3) with $\lambda_x = 3$, $\lambda_y = 1.5$: dark for the basin of $y = -\infty$, blank for the basin of $y = +\infty$. (b) Magnification of the region $0.38317 \le x \le 0.38327$, $0.4450 \le y \le 0.4451$ revealing striated boundary structure.

there are λ_x (an integer) inverses of each point x_n: $x_{n-1}^{(j)} = (j + x_n)/\lambda_x$, $j = 0, \ldots, \lambda_x - 1$. Once a particular inverse of x_n is chosen, the inverse y_{n-1} is determined from (5.3b) as

$$y_{n-1} = \frac{1}{\lambda_y}(y_n - \cos 2\pi x_{n-1}). \tag{5.5}$$

Each of the inverse sequences $\{(x_n, y_n), (x_{n-1}, y_{n-1}) \ldots\}$ must approach the basin boundary.

The construction of the basin boundary now proceeds as follows: First, we select an initial value x_0 at which we wish to determine the corresponding y value for the boundary, $y_0 = B(x_0)$. Noting that the evolution (5.3a) of the x-coordinate is independent of y, we iterate x_0 N times to produce the one-dimensional x-orbit $\{x_0, x_1, \ldots, x_N\}$, where $x_n = \lambda_x^n x_0$ (mod 1). Now choose an arbitrary value of y_N to pair with the final point x_N in order to determine the point (x_N, y_N) in the plane. There are λ_x^N orbits which result in (x_N, y_N) after N steps; one of these must begin with initial value $x = x_0$ and proceed along the x-orbit already constructed. Thus, we can form the particular inverse sequence which begins at (x_N, y_N) and ends at (x_0, y_0) by using repeated applications of (5.5) to determine the y_n, since all the x_n are known. For example, we have

$$\begin{aligned} y_{N-1} &= \frac{1}{\lambda_y}(y_N - \cos 2\pi x_{N-1}) \\ &= \frac{1}{\lambda_y} y_N - \frac{1}{\lambda_y}\cos\left(2\pi\lambda_x^{N-1}x_0\right), \\ y_{N-2} &= \frac{1}{\lambda_y^2} y_N - \frac{1}{\lambda_y^2}\cos\left(2\pi\lambda_x^{N-1}x_0\right) \\ &\quad - \frac{1}{\lambda_y}\cos\left(2\pi\lambda_x^{N-2}x_0\right). \end{aligned} \tag{5.6}$$

Thus the expression for y_0 is

$$y_0 = \frac{y_N}{\lambda_y^N} - \sum_{j=1}^{N} \lambda_y^{-j}\cos\left(2\pi\lambda_x^{(j-1)}x_0\right), \tag{5.7}$$

and, letting $N \to \infty$, we see that the basin boundary is

$$y = B(x) = -\sum_{j=1}^{\infty} \lambda_y^{-j}\cos\left(2\pi\lambda_x^{j-1}x\right). \tag{5.8}$$

As discussed in section 3.3, this expression implies that the basin boundary $B(x)$ is a continuous, nowhere differentiable curve (but not a quasicircle). For a check on our numerical procedure for measuring the uncertainty exponent α, we have applied it to the case shown in fig. 19 ($\lambda_x = 3$, $\lambda_y = 1.5$). The resulting value $\alpha \approx 0.38$ compares well with that given by the expression for the capacity dimension (see section 3.3): $\alpha = D - d = 2 - d = (\ln\lambda_y/\ln\lambda_x) = 0.37\ldots$ in this case.

We have presented now two examples of locally connected fractal basin boundaries. The typical boundary for a quadratic analytic map (see fig. 4) was described as possessing a "snowflake" structure, whereas the fractal boundary for the map (5.3) exhibits a "striated" or stretched shape. In order to explain the difference between the boundary of fig. 19 and that of fig. 4, we consider the composed linear map

$$\begin{aligned} \delta\boldsymbol{x}_{-n} &= \mathrm{TM}^{-1}(\boldsymbol{x}_{-n+1}) \\ &\quad \cdot \mathrm{TM}^{-1}(\boldsymbol{x}_{-n+2}) \cdot \cdots \cdot \mathrm{TM}^{-1}(\boldsymbol{x}_0) \cdot \delta\boldsymbol{x}_0 \\ &\equiv \boldsymbol{L}^{(-n)}(\boldsymbol{x}_0) \cdot \delta\boldsymbol{x}_0, \end{aligned} \tag{5.9}$$

where $\boldsymbol{x} = (x, y)$, $\delta\boldsymbol{x} = (\delta x, \delta y)$, and each matrix $\mathrm{TM}^{-1}(\boldsymbol{x}_j)$ is given by the inverse of (5.4) evaluated at the point $\boldsymbol{x}_j$ along any of the λ_x^n inverse orbits of length n generated from $\boldsymbol{x}_0$. From (5.4) we have

$$\mathrm{TM}^{-1}(\boldsymbol{x}_j) = \begin{pmatrix} \lambda_x^{-1} & 0 \\ \dfrac{2\pi\sin 2\pi x_j}{\lambda_x\lambda_y} & \lambda_y^{-1} \end{pmatrix} \tag{5.10}$$

and therefore $\boldsymbol{L}^{(-n)}$ is of the form

$$\boldsymbol{L}^{(-n)}(\boldsymbol{x}_0) = \begin{pmatrix} \lambda_x^{-n} & 0 \\ A_n(\boldsymbol{x}_0) & \lambda_y^{-n} \end{pmatrix}. \tag{5.11}$$

The eigenvalues of $\boldsymbol{L}^{(-n)}$ are $(\lambda_x^{-n}, \lambda_y^{-n})$. Therefore, the Lyapunov numbers for any inverse sequence of (5.3), as defined in (5.2), are

$$\mu_1^- = \lambda_x > \mu_2^- = \lambda_y > 1. \tag{5.12}$$

Due to the inequality of the two eigenvalues the action of $\boldsymbol{L}^{(-n)}$ on a small disk at $\boldsymbol{x}_0$ produces a highly eccentric ellipse with length-to-width ratio of the order of $(\lambda_x/\lambda_y)^n$. This results in the structure of fig. 19. This is in contrast to the case of analytic maps for which the Cauchy–Riemann structure implies that an initial disk remains a disk upon iteration (implying that the two Lyapunov numbers of the map are equal). This is manifested in the "snowflake" structure of the Julia set in fig. 4.

5.3. *Nonanalytic noninvertible quadratic maps on the plane*

The previous examples of fractal curve basin boundaries have arisen in very special cases of two-dimensional maps. The class of analytic maps is special because of the Cauchy–Riemann relations. The map given in eq. (5.3) is also special in that the eigenvalues of the tangent map are independent of x and y, and one can construct the explicit form of the basin boundary. Thus, in order to investigate the properties of basin boundaries one might expect to exist in typical dissipative dynamical systems, we consider in this subsection more general maps of the plane, which have none of the special qualities discussed above.

We shall restrict our attention to quadratic maps of the plane

$$\begin{aligned} x_{n+1} &= a_{xx}x_n^2 + a_{xy}x_ny_n + a_{yy}y_n^2 + a_xx_n \\ &\quad + a_yy_n + a_c, \qquad (5.13) \\ y_{n+1} &= b_{xx}x_n^2 + b_{xy}x_ny_n + b_{yy}y_n^2 + b_xx_n + b_yy_n + b_c. \end{aligned}$$

In general, a map of this form is noninvertible and can therefore be argued to exhibit properties found in systems of higher dimension. Examples of (5.13), such as the Hénon map (which is invertible), have been studied and have been shown to possess chaotic attractors. Also, since analytic maps are a subset of the class (5.13), one might expect general quadratic maps to exhibit fractal boundaries. Thus, we expect that, in general, (5.13) can have both fractal basin boundaries and chaotic attractors. Our results lead us to believe that striated fractal basin boundaries are "common" while the snowflake structure fractal basin boundaries found in analytic maps are not. By this we mean that, if coefficients of (5.13) are chosen randomly from some ensemble with a continuous probability density, then the probability of obtaining a map with a striated fractal basin boundary would be positive, while the probability of a map with a snowflake structure fractal basin boundary would be zero. (We also find smooth basin boundaries to be common.)

Surveying the twelve-dimensional parameter space of (5.13) in search of fractal boundaries and chaotic attractors is clearly an inordinately large task. Therefore, we begin with an analytic map

$$\begin{aligned} x_{n+1} &= x_n^2 - y_n^2 + \tfrac{1}{2}x_n - \tfrac{1}{2}y_n, \\ y_{n+1} &= 2x_ny_n + \tfrac{1}{2}x_n + \tfrac{1}{2}y_n. \end{aligned} \tag{5.14}$$

This map has an attracting fixed point at the origin and an attractor at infinity; the basin boundary shown in fig. 20 is fractal, though somewhat less spectacular than that in fig. 4. We then alter this map to be nonanalytic by changing the coefficients of the linear terms and adding constant terms until a map with a chaotic attractor is found. Such a map is given by

$$\begin{aligned} x_{n+1} &= x_n^2 - y_n^2 + x_n - 0.297y_n + 0.048, \\ y_{n+1} &= 2x_ny_n + x_n - 0.6y_n. \end{aligned} \tag{5.15}$$

The structure of this map, shown in fig. 5, is studied in more detail in ref. 23. Again, initial conditions in the dark region escape to infinity; in this case, however, orbits in the interior blank region approach a chaotic attractor which is also

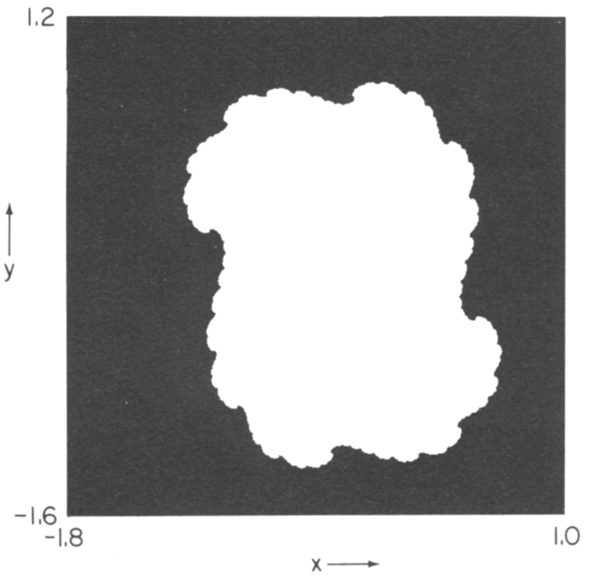

Fig. 20. Basin structure for the analytic map given in eqs. (5.14): dark for the basin of infinity, blank for the basin of the fixed point at the origin.

displayed. This attractor (here constructed from a single initial condition) contains self-intersections due to the noninvertibility of (5.15).

On the scale of fig. 5a, the basin boundary appears to be characterized by roughly self-similar whorls repeated with varying size and distortion around the boundary at intervals which seem to accumulate near the point labeled A in the lower right-hand corner. This is the location of an unstable fixed point. The tangent map at this fixed point has complex conjugate eigenvalues of magnitude greater than one. Thus, in the vicinity of this fixed point the map is expanding and rotating; this behavior of the boundary near the fixed point is revealed under repeated magnification. This structure replicated around the boundary has long spiral arms (see fig. 5b). As the coefficient a_y in (5.15) is varied, the attractor is observed to collide with these arms in a "crisis" [3, 23], destroying the attractor and its basin.

The microscopic structure at a representative location on the boundary is shown in fig. 5c. This magnification by a factor of 10^7 exposes local linear striations similar to that found for eq. (5.3) (see fig. 19). Further magnification of any of the interfaces between dark and blank in fig. 5c produces a similar picture of striations on smaller scale, although the pattern of transversal spacing may not be the same. Apparently, the magnification of almost any small region around the boundary will reveal such structure; the degree of magnification required before this structure is apparent, however, may depend on the location. Thus, the "rotating" structures on large scale are ultimately replaced on finer scale by striations indicating local stretching. An interpretation connecting these observations would be that the local leaves or layers are just the flattened extensions of many greatly stretched spiral arms in the neighborhood of some small whorl. This is roughly displayed on a large scale in the structure of the object labelled B emanating from the spiral fixed point at A in fig. 5a.

The result to be emphasized here is that a non-special choice of parameters for a two-dimensional quadratic map can produce either a smooth boundary or a boundary with a fractal character of local striations as opposed to the "snowflake" pattern of analytic maps. The uncertainty exponent α for fig. 5 is approximately 0.7. This would indicate a fractal dimension of 1.3, using (2.4).

The "striations" of the boundary in this example are reminiscent of the simple model for this behavior provided by (5.3) of the previous subsection. In that case, the linear structure was interpreted in terms of the Lyapunov numbers of the inverse mapping. That model is simple, however, in that not only can one calculate this effect, but the stretching occurs in the same direction (y) independent of location on the boundary and the Lyapunov numbers are independent of inverse path. Here, no analytic calculation of Lyapunov numbers is possible. Thus, a numerical computation of inverse orbits and corresponding Lyapunov numbers (which now will depend on the inverse sequence chosen) is required to investigate this connection. This will be discussed in section 6.

In addition to this single example (5.15), we have surveyed many other noninvertible quadratic maps of the class (5.13). We restricted our attention to those maps for which the origin is a fixed point, $a_c = b_c = 0$. Furthermore, we considered only the cases in which the origin is unstable so that either some other finite attractor exists of almost all orbits escape to infinity. For each case considered in this class, we examined the orbits generated by 63 initial conditions in the neighborhood of the origin; if all of these did not tend to infinity, we concluded that for this case a finite attractor must exist. Sampling 6400 maps in this way, we found that roughly 17% of the cases satisfied this condition for possessing multiple attractors. From this collection of approximately 1000 maps, we selected several random examples for further investigation of their basin boundaries. On this basin, our findings can be summarized as follows:

1) In general, a quadratic noninvertible map of the plane may possess multiple attractors with a basin boundary which can either be a smooth curve or a fractal.

2) In the case of a fractal curve basin boundary, the local fractal structure generally exhibits linear striations (as opposed to the "snowflake" pattern of analytic maps).

Thus we believe that small-scale, striated structure in fractal basin boundaries should commonly occur, but that the small-scale, snowflake, two-dimensional structure of complex analytic maps is very special and should not occur in typical situations.

6. Lyapunov numbers and dimension for the measure on fractal basin boundaries

6.1. *Lyapunov numbers for inverse orbits*

Here we discuss the Lyapunov numbers as applied to the examples of locally-connected basin boundaries in two-dimensional maps considered in the previous section. In particular, we consider the Lyapunov numbers for an orbit generated by inverse images of an initial point in the vicinity of the basin boundary (such points are attracted to the boundary). Since the maps which we discuss in this section do not have a unique inverse, we need a rule for choosing which preimage of a point is to be on the inverse orbit. Here we shall choose the preimage at random with equal probability for each of the possible preimages. In our numerical calculations of Lyapunov numbers, we do this by making use of a random number generator. An orbit produced in this way will generate an asymptotic measure on the basin boundary. We conjecture that this measure is the same for almost all initial conditions in any neighborhood of the boundary for which almost all inverse orbits are attracted to the boundary. We call the measure generated by random choices of preimages the *natural measure* for the basin boundary.

Fig. 21 depicts the result of plotting 200,000 inverse iterates for the map of fig. 5 of the previous section. The distribution of points on the boundary appears to be extremely nonuniform, emphasizing certain regions very heavily, while leaving others comparatively unexplored. We numerically obtain the smallest Lyapunov number by finding the largest eigenvalue of the composition of the inverse tangent map along the inverse orbit (cf. eq. (5.2)). Due to the finite precision of numerical computations, the largest Lyapunov number μ_1^- is usually inaccurately given by the smallest eigenvalue of the composed inverse tangent map. Therefore, in order to compute it we take products

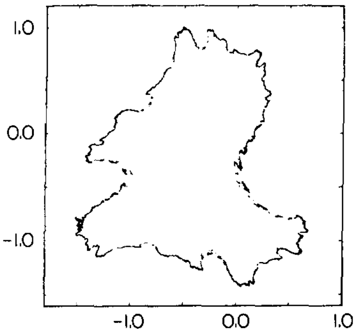

Fig. 21. Inverse orbit on the boundary of fig. 5 (eqs. (5.15)) with 200,000 iterations. At each stage of the inverse iteration, the choice between two possible preimages was made at random.

of the determinant of the individual tangent maps along the inverse orbit to obtain the determinant of the N-times composed inverse tangent map. Since this determinant is equal to the product of the eigenvalues of the composed matrix, and since we know the largest eigenvalue, we thus determine the smallest eigenvalue.

We emphasize that the Lyapunov numbers that we obtain in this way are Lyapunov numbers appropriate to the natural measure generated by the inverse orbit. That is, the stretching properties of those regions of the boundary with larger measures are more strongly weighted in the calculation of the Lyapunov numbers than are those regions with smaller measures.

For the three examples discussed in section 5 we have the following results for the Lyapunov numbers:

1) For the analytic map of fig. 4, a numerical calculation of the Lyapunov numbers (both are equal for analytic maps) yields $\mu_{1,2}^{-}=2$ to within numerical accuracy (± 0.01).

2) For the map (5.3), it is easy to show that $\mu_1^- = \lambda_x$ and $\mu_2^- = \lambda_y$.

3) For the map of fig. 5 we numerically obtain $\mu_1^- = 2.15$ and $\mu_2^- = 2.09$.

6.2. *Dimension of the measure for fractal basin boundaries*

For the case of chaotic *attractors*, a formula for the dimension of the measure on the attractor has been conjectured [12, 22] and gives correct results in examples where the dimension of the measure is known. For a discussion and definitions of the dimension of the measure see Farmer, Ott, and Yorke [12]. In this subsection we develop an analogous conjecture for the dimension of the natural measure generated by inverse orbits on a fractal basin boundary. For definiteness in this discussion, we assume that almost all points on the boundary have two preimages. This assumption is, in fact, satisfied by our examples of figs. 4 and 21, and is also satisfied by eqs. (5.3) if $\lambda_x = 2$. The heuristic arguments leading to our expression for the dimension of the natural measure of these basin boundaries (eq. (6.1)) are similar to those for the previous development for the case of chaotic attractors; the main difference is that here we need to account for the fact that there are two preimages for points on the boundary.

Say we have an initial set of N_0 small squares of side ε_0 covering the boundary. Now apply the inverse map n times to each square on the boundary. Each square will be mapped to 2^n small parallelograms, typically with length of the order of $\varepsilon_0/(\mu_2^-)^n$ and width of the order of $\varepsilon_0/(\mu_1^-)^n$ (we assume that both μ_1^- and μ_2^- are larger than one). Since the boundary is invariant, the collection of these $2^n N_0$ parallelograms also covers the basin boundary. We can typically cover each parallelogram with of the order of $(\mu_1^-/\mu_2^-)^n$ small boxes of side $\varepsilon_n \equiv \varepsilon_0/(\mu_1^-)^n$. Thus, if we assume that it takes $N(\varepsilon) \sim \varepsilon^{-d}$ boxes of side ε to cover the boundary, then

$$N(\varepsilon_0)/N(\varepsilon_n) = \left[2(\mu_1^-/\mu_2^-)\right]^{-n} = (\varepsilon_n/\varepsilon_0)^d = (\mu_1^-)^{-nd}.$$

Thus taking logarithms, we obtain

$$d_{\mathrm{L}} = 1 + \left[\ln(2/\mu_2^-)\right]/\ln\mu_1^-, \tag{6.1}$$

where the subscript L denotes that (6.1) is a prediction based on the Lyapunov numbers, and we call d_{L} the Lyapunov dimension of the boundary. Since the Lyapunov numbers reflect behavior for points on the boundary weighted by the natural measure on the boundary, we conjecture that d_{L} is equal to the dimension of the natural measure of the boundary (which is usually not the same as the capacity dimension). See ref. 12 for further discussion.

For the case of the analytic map of fig. 4, $\mu_1^- = \mu_2^- = 2$ yields $d_{\mathrm{L}} = 1$. This is in agreement with the rigorous theoretical result of Manning [24] for Julia sets of polynomial analytic maps. Note, however, that the capacity dimension as measured by the final state sensitivity exponent α is approximately $1.3 > 1$. For fig. 4, this may be viewed as a reflection of the fact that the measure generated by randomly chosen inverse iterates is highly concentrated on a set of lower dimension than the capacity of the boundary. The situation is very similar for the case of the boundary shown in fig. 5 for a nonanalytic quadratic map. In that case our numerically calculated Lyapunov numbers yield $d_L \approx 0.94$, while the final state sensitivity exponent yields a capacity dimension of about 1.3. For the case of the boundary for the map (5.3) with $\lambda_x = 2$, (6.1) yields

$$d_L = 2 - \frac{\ln \lambda_y}{\ln 2},$$

in agreement with the rigorous result of Kaplan, Mallet-Paret and Yorke [14].

7. Conclusions

Basin boundaries for typical dynamical systems can be expected to be either smooth or fractal. In this paper we have investigated fractal basin boundaries. Our main conclusions are as follows:

1) Fractal basin boundaries can strongly affect the ability of predicting to which attractor a system eventually goes. In particular, a substantial reduction in the error in the initial condition can, under some circumstances, lead to only modest increase in predictive ability (section 2).

2) Fractal basin boundaries can be classified as being either locally disconnected or locally connected (section 3).

3) Examples of locally disconnected basin boundaries resulting from horseshoe type dynamics appear to be common (section 4).

4) Locally connected basin boundaries may or may not be quasicircles (section 3). Quasicircle basin boundaries, as exemplified by analytic mappings of a single complex variable, however, appear to be very special and are not to be expected in general (section 5). As a result, fine scale structure of locally connected boundaries should, most commonly, exhibit a one-dimensional (or striated) appearance (e.g., fig. 5), rather than a two-dimensional (or snowflake) appearance (e.g., fig. 4).

5) The dimension of the measure generated by inverse orbits on a fractal basin boundary and its possible connection with the associated Lyapunov numbers has been discussed (section 6).

Acknowledgements

This work was supported by the Air Force Office of Scientific Research, the Department of Energy (Office of Scientific Computing), the National Science Foundation, and the Office of Naval Research.

Appendix A

$\alpha = 1$ Basin boundaries with $f(\varepsilon)$ not proportional to ε

In this appendix we consider basin boundaries for which $\alpha = 1$ according to our definition (2.7), but for which $f(\varepsilon) \doteq k\varepsilon$ for small ε does not hold. In particular, consider the example in fig. 22a. This figure shows two basins of attraction (the dark and blank regions) for the Hénon map at parameter values such that the map has two distinct strange attractors. The map corresponding to this figure is given by $x_{n+1} = 1 - 1.0807x_n^2 + y_n$, $y_{n+1} = 0.3\ x_n$. Fig. 22b shows a magnification of the boxed region in fig. 22a and fig. 22c is a further magnification of the boxed region in fig. 22b. The replication evident on comparison of figs. 22b and 22c is *not* a consequence of fractal structure, but rather of the fact that an unstable saddle fixed point is located in the center of these figures. Indeed, the basin boundary here is a smooth curve with dimension one.

To understand how the structure illustrated in figs. 22 arises, consider the stable and unstable manifolds of the fixed point (FP), as shown in fig. 23. The stable manifold (shown as a dashed line in

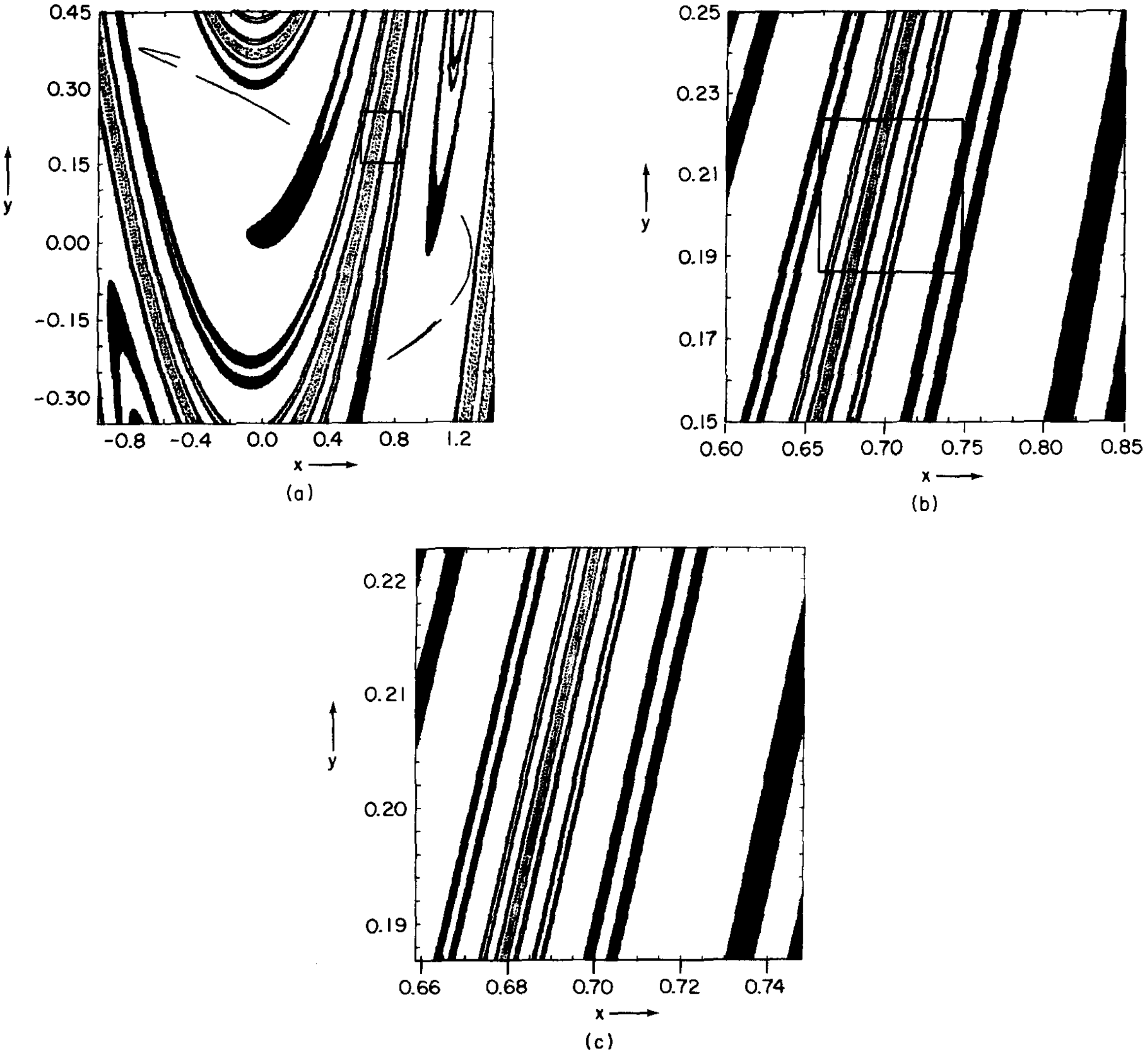

Fig. 22. (a) Basin structure of the Hénon map at parameter values for which both a four-piece chaotic attractor (shown, with blank basin) and a six-piece chaotic attractor (not shown, dark basin) exist. Figs. 22a–c adapted from the second of ref. [3]. (b) Magnification of rectangle in (a). The vertical bands accumulate (transversally, along the unstable manifold) at the piece of the stable manifold (cf. fig. 22) running vertically just left of center in the small rectangle; indeed, the fixed point FP in fig. 25 is in this small rectangle. (c) Magnification of small rectangle in (b) by a factor λ_u^2.

fig. 23) is in the direction along the bands in fig. 22, while the unstable manifold cuts across them. In particular, the bands accumulate at the piece of the unstable manifold shown dashed in fig. 23. The stable and unstable eigenvalues of the Jacobian matrix at the fixed point are $\lambda_s = 0.17931\ldots$ and $\lambda_u = -1.6731\ldots$. Now consider the application of the inverse mapping to fig. 22b. Bands crossing the unstable manifold will be drawn in toward the fixed point, contracted in width (by approximately $|\lambda_u|^{-1}$), flipped to the other side of the fixed point (because λ_u is negative), and stretched out along the stable manifold (by λ_s^{-1}). In fact, fig. 22c is a magnification of fig. 22b by precisely the amount λ_u^2 (corresponding to two applications of the inverse map).

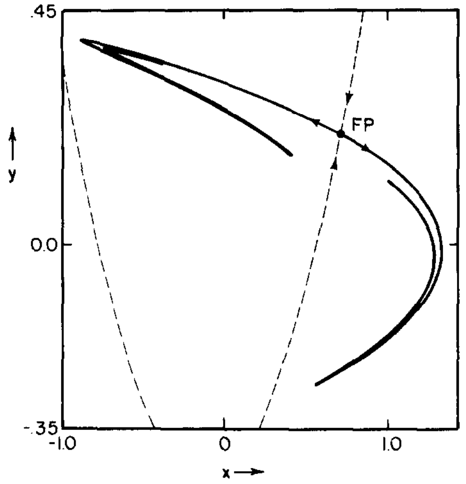

Fig. 23. Pieces of the stable (dashed) and unstable (solid) manifolds of the unstable fixed point (FP) in the Hénon map. Adapted from the second of ref. [3].

We now consider fig. 22b and attempt to deduce how the uncertain fraction of this region behaves for small initial error ε. First we note that the phase space in fig. 22b that is within ε of the dashed portion of the stable manifold of FP shown in fig. 23 is uncertain. We now wish to estimate the volume of the uncertain phase space that is outside this inner strip. Since, for small ε this volume will turn out to be larger than the volume of the strip itself, it is the outside region which will determine $f(\varepsilon)$. In order to estimate the number of boundary lines outside the inner strip, we first note that all of the boundary lines outside the inner strip in fig. 22b can be regarded as being generated (via inverse mapping) from the four outermost boundary lines. Say we consider these four outermost lines and apply the inverse map to them until they first fall within the inner strip of width ε. Call the number of iterates necessary to do this r. If w is the x-width of fig. 22b, in order of magnitude we have

$\varepsilon/w \sim |\lambda_u|^{-r}$. Thus,

$$r \cong K_1 \ln(1/\varepsilon),$$

for small ε, where K_1 is a constant. Since by construction these boundary lines that are outside the inner strip are all separated by distances of the order of ε or greater, we have that for small ε, $f(\varepsilon)$ is proportional to $r\varepsilon$ or

$$f(\varepsilon) \cong K_2 \varepsilon \ln(1/\varepsilon). \tag{A.1}$$

Other examples also exist. In particular, if one considers the final phase sensitivity (cf. section 4.2-1) of the period two orbit for the logistic map (in the parameter range below that at which period doublings accumulate), then one finds $f(\varepsilon) \cong K_3 \ln(1/\varepsilon)$. As in the case of figs. 22, the reason for this behavior involves a period one unstable fixed point.

References

[1] E. Ott, Rev. Mod. Phys. 53 (1981) 655; and references therein.
[2] C. Grebogi, S.W. McDonald, E. Ott and J.A. Yorke, Phys. Lett. 99A (1983) 415.
[3] C. Grebogi, E. Ott and J.A. Yorke, Phys. Rev. Lett. 48 (1982) 1507; Physica 7D (1983) 181.
[4] C. Grebogi, E. Ott and J.A. Yorke, Phys. Rev. Lett. 50 (1983) 935.
[5] M.L. Cartwright and J.E. Littlewood, Ann. Math. 54 (1951) 1; J. London Math. Soc. 20 (1945) 180.
[6] N. Levinson, Ann. Math. 50 (1949) 127.
[7] M. Levi, Mem. Amer. Math. Soc. 32 (1981) 244.
[8] J.L. Kaplan and J.A. Yorke, Comm. Math. Phys. 67 (1979) 93.
[9] E.N. Lorenz, J. Atmos. Sci. 20 (1963) 130.
[10] T.-Y. Li and J.A. Yorke, Am. Math. Mon. 82 (1975) 985.
[11] G. Julia, J. Math. Pure Appl. 4 (1918) 47. P. Fatou, Bull. Soc. Math. France 47 (1919) 271. B.B. Mandelbrot, Ann. N.Y. Acad. Sci. 357 (1980) 249.
[12] J.D. Farmer, E. Ott and J.A. Yorke, Physica 7D (1983) 153.
[13] S. Pelikan, "A Dynamical Meaning of Fractal Dimension," U. Minn. IMA Preprint #73 (1984).
[14] J.L. Kaplan, J. Mallet-Paret, and J.A. Yorke, Ergod, Th.& Dyn. Sys. 4 (1984) 261.
[15] S. Smale, Bull. Amer. Math. Soc. 73 (1967) 747.
[16] J.E. Flaherty and F.C. Hoppensteadt, Stud. Appl. Math. 58 (1978) 5.

[17] J. Guckenheimer and P. Holmes, Nonlinear Oscillations, Dynamical Systems, and Bifurcation of Vector Fields, Appl. Math. Sci. vol. 42 (Springer, New York, 1983).

[18] S. Smale and R.F. Williams, J. Math. Biol. 3 (1976) 1.

[19] G. Pianigiani and J.A. Yorke, Transactions Amer. Math. Soc. 252 (1979) 351.

[20] J.A. Yorke and E.D. Yorke, J. Stat. Phys. 21 (1979) 263.

[21] P. Bergé and M. Dubois, Phys. Lett. 93A (1983) 365.

[22] J.L. Kaplan and J.A. Yorke, in: Functional Differential Equations and Approximation of Fixed Points, Lecture Notes in Math. vol. 730 (Springer, New York, 1979) p. 228.

[23] S. McDonald, C. Grebogi, E. Ott and J.A. Yorke, Phys. Lett. 107A (1985) 51.

[24] A. Manning, Ann. Math. 119 (1984) 425.